ALTERNATE METHODS TO DETERMINE THE MICROSTRUCTURE OF POTENTIALLY COLLAPSIBLE SOILS

By

Asante Samuel Yaw

Dissertation presented for the degree of Master of Engineering in the Faculty of Engineering at Stellenbosch University

Supervisor: Mrs. Nanine Fouché
Lecturer in Geotechnical Engineering
Department of Civil Engineering
Faculty of Engineering

December, 2015

DECLARATION

By submitting this thesis electronically, I declare that the entirety of the work contained therein is my own, original work, that I am the sole author thereof (save to the extent explicitly otherwise stated), that reproduction and publication thereof by Stellenbosch University will not infringe any third party rights and that I have not previously in its entirety or in part submitted it for obtaining any qualification.

December 2015

i

ABSTRACT

Collapsible soil is one of the most widely distributed problematic soils in the world including South Africa. Extreme leaching and erosion of the colloidal matter and fine particles creates a structure similar to a honeycomb within the microstructure of these soils, leading to the formation of a collapsible grain structure. Upon wetting and under additional loading these soils undergo a significant decrease in volume resulting in severe damage to structures. In South Africa the collapse phenomenon, which is regarded a geotechnical hazard, was first identified in the 1950's.

According to Rogers (1995), a geotechnical engineer needs to be able to identify these soils by examining in detail the properties of collapsible soils by listing the features commonly associated with it; which includes:

- An open soil structure;
- A high void ratio;
- A low dry density;
- A high porosity;
- Geologically young or recently altered deposit;
- High sensitivity and
- Low inter-particle bond strength.

The first four features suggested by Rogers (1995) suggest that the collapse phenomenon is directly controlled by the microstructure of these collapsible soils.

From Rogers's definition, it can be concluded that the microstructure of collapsible soils are governed by the following: porosity, pore size distribution, grain size distribution, pore fluid content, and ions on the grain and in pores (mechanical properties). Each of these microstructure properties can be examined and/or determined by laboratory testing or field observation.

For this reason, the collapse behaviour of two soil types (reworked residual granite and residual Malmesbury shale) within the Stellenbosch municipal area was investigated by examining the

microstructure and mechanical behavior of these soils. Alternate methods (CT-scanning and scanning electron microscopy) as well as conventional laboratory tests were applied.

The aims of the study was achieved by developing a soil testing method using x-ray computed tomography (CT-scanning) and scanning electron microscopy (SEM) to determine the porosity, void ratio, particle size distribution, particle shape, and pore size distribution of residual soils. In order to achieve this, the VGStudio Max version 2.2 coupled together with Avizo Fire image analysis software version 8.0 were used in filtering and classification and distribution of voids, and particle size distribution within the soil microstructure. The image analysis was achieved by examining three dimensional (3D) and two dimensional (2D) X-ray images obtained using a General Electric Phoenix VTomeX L240 X-ray micro computed tomography scanner (microCT) and ZEISS EVO MA15 scanning electron microscope.

From the image analysis, it was found that substantial volumetric changes (settlement) occur within the macropores of a potentially collapsible soil. The measured particle size distribution (PSD) by CT-scanning compared relatively well with the mechanical sieving method, although a few discrepancies were noted between the two methods. The image analysis from the SEM 2D images revealed that the particle morphology and mineralogy contributed greatly to the degree of collapse. The PSD from SEM images using imageJ (image analysis software) was not possible due to the bleeding effect of fine to medium-sized particles. It can thus be concluded that CT-scanning and SEM are good alternative methods to investigate the microstructure of soils; and further research in this regard is indicated.

OPSOMMING

Swigbare grond is die mees algemene soort problematiese grond in die wêreld insluitende Suid-Afrika. Ernstige uitloging en erosie van die lymagtige stof en die fyner partikels skep 'n struktuur wat soortgelyk is aan 'n heuningkoek in die mikrostruktuur van hierdie grondtipes. Dit lei tot die formasie van 'n korrelstruktuur wat geneig is om in te sak.   As dit nat word en as daar addisionele las op die grond geplaas word, verminder die volume van die grond, wat lei tot skade aan die struktuur. Hierdie verskynsel, wat as 'n geotegniese gevaar beskou word, is vir die eerste keer in die vyfigerjare geïdentifiseer.

Volgens Rogers (1995) moet 'n geotegniese ingenieur hierdie tipe grond kan identifiseer deur die kenmerke van grond wat geneig is om in te sak, te identifiseer en die kenmerke wat daarmee geassosieer word, te lys. Hierdie kenmerke sluit die volgende in:

- 'n Oop grondstruktuur;
- 'n Hoë tussenkorrelporie-verhouding;
- 'n Lae droë digtheid;
- Hoë poreusheid;
- Geologiese jong of onlangs veranderde neersetting;
- Hoë sensitiwiteit en
- Lae interpartikelverbindingsterkte

Die eerste vier kenmerke wat deur Rogers (1995) genoem word, wys daarop dat die swigversakking direk van die mikrostruktuur van die grond afhang.

Volgens Rogers se definisie kan daar afgelei word dat die mikrostruktuur van grond wat swigbaar is, afhang van die volgende: poreusheid, die verspreiding van die grootte van die porieë, die verspreiding van greingroottes, die vloeistof inhoud van die porieë, en die ione op die korrels en in die openinge (meganiese kenmerke).   Elkeen van hierdie mikrostruktuur-kenmerke kan deur laboratoriumtoetsing of veldwaarneming ondersoek en/of vasgestel word.

Daarom is die swigversakking van twee grondtipes (residuele graniet en residuele Malmesbury skalie) in die Stellenbosch munisipale gebied ondersoek. Die mikrostruktuur en die meganiese

gedrag van die grondtipes is ondersoek. Alternatiewe metodes (CT-skandering en skanderingselektronmikroskopie, SEM) asook konvensionele laboratorium-toetsing is gebruik.

Die doel van hierdie studie is bereik deur 'n grondtoetsingmetode te ontwikkel wat x-straal berekende tomografie (CT skandering) en SEM insluit. Die doel was om die poreusheid, die openingverhouding, die verspreiding van partikelgroottes, die vorm van die partikels en die verspreiding van die openinggroottes vas te stel. Om hierdie doel te bereik is die VGStudio Max weergawe 2.2 tesame met "Avizo Fire image analysis" sagteware weergawe 8.0 gebruik vir die filtrering en klassifikasie van openinge en die verspreiding van partikelgrootte in die mikrostruktuur van die grond. Die beeldontleding is gedoen deur drie-dimensionele (3D) en twee-dimensionele (2D) X-straal beelde te ondersoek wat met 'n General Electric Phoenix VTomeX L240 X-straal mikro berekende tomografiese skandeerder (microCT) en 'n ZEISS EVO MA15 elektronmikroskoop gedoen is.

Daar is deur middel van hierdie ontleding bevind dat redelike groot veranderinge in volume plaasvind in die openinge van 'n potensieël swigbare grond. Die verspreiding van partikel-grootte soos deur skandering gemeet vergelyk redelik goed met die bevindings van die meganiese sifmetode, maar daar is wel 'n paar verskille in die bevindinge. Die ontleding van die SEM 2D-beelde toon dat die partikelmorfologie en mineralogie grootliks bydra tot die mate van insakking. Die PSD van die SEM beelde deur die gebruik van beeld-ontledingsagteware was weens die bloei-effek van fyn tot mediumgrootte partikels, nie moontlik nie. Daar is dus bevind dat CT skandering en SEM goeie alternatiewe metodes is vir die ondersoek van die mikrostruktuur van grond en ander soortgelyke navorsing.

ACKNOWLEDGEMENT

First and foremost, I would like to thank to thank God for the inspiration and his protection throughout my stay in South Africa.

Gratitude also goes to National Research Foundation (NRF), South Africa for their sponsorship for the entire program.

The quality of my thesis wouldn't have been possible without the continual guidance, support, valuable insights and useful comments from my supervisor; Mrs. Nanine Fouché. All I can say is, God bless you.

My sincere gratitude also goes to Mr. Abraham Asante-Manteaw, Miss Beatrice Asante, Dr. Suvash Paul, Dr. Asare-Asher Samuel, and my office mates.

With regards to CT scan, and SEM analysis; I would like to thank Dr. Aton du Plessis, Mr. Stephan Le Roux , Mr. James Olawuyi and Miss Madelen Franzenburg for their support and guidance.

I would like to acknowledge the contribution of Ernie Els Wines, and Boland Bricks for granting me the permission to work on their premises.

TABLE OF CONTENTS

Contents

LIST OF FIGURES

LIST OF TABLES

CHAPTER 1. INTRODUCTION

1.1   BACKGROUND

Collapsible soils are known to be one of the problematic soils in some areas of the world including South Africa. The collapse phenomenon can have devastating effects on foundations of buildings, roads, earth dams, and railways. By definition, collapsible soil exhibits a collapsible grain structure which can withstand relatively large imposed stresses with small settlements at a low in-situ moisture content, but will display a decrease in volume upon wetting (Schwartz, 1985). For collapse to occur, the first condition to be met is the presence of a collapse fabric (Schwartz, 1985). Brink et al. (1982) further indicated the following: " a collapsible fabric may occur in any open textured silty or sandy soil, which has a high void ratio (low dry density) and yet has relatively high shear strength at low moisture content due to colloidal or other coatings around the individual grains. In the South African context, this is common in many transported soils and also in areas where quartz-rich rocks such as granite or feldspathic sandstone have undergone chemical weathering to produce intensely leached residual soils."

The definition of a soil with a collapse fabric as suggested by Brink et al. (1982) implies that the microstructure of collapsible soils is governed by: porosity, pore size distribution, grain size distribution, pore fluid content, ions on particle grains and in the pores. These can be determined either by laboratory testing methods or by field observation. The laboratory tests are classified as either destructive or non-destructive. Destructive techniques include particle size analysis, collapse potential tests and tests to determine the Atterberg limits. On the other hand, non-destructive techniques include X-ray computed tomography (CT-Scan), electron microscopy, ultrasonic testing, and acoustic sounding (Alshibi et al., 2000).

Although, the use of computed tomography scanning and scanning electron microscopy techniques in geotechnical engineering is still under development, it is showing promising growth with increasing research development.

An experimental analysis conducted by Neilsen (2004), provided a useful approach for measuring the microstructure of granular soils. The porosity and grain size distributions were determined by

1

image analysis based on pixel intensity from image analysis software without any hardening agents. As a result, minimal or absolutely no sample disturbance occurred. The non-destructive nature of the CT scan allows the same soil sample to be scanned several times. Since samples will not be affected by the testing, CT scanning provides an opportunity to investigate particle and pore interactions at any time and location (Nielsen, 2004).

Scanning electron microscopy, although with some primary limitations such as sample preparation, has become a basic technology that can be deployed in the investigation of soil microstructure (Remley 1989, Sullivan, 1990). Particle sizes ranging from several millimeters to hundreds of nanometers can be determined successfully, (Nenadović et al. 2010). In addition, recent investigations conducted using scanning electron microscopy, also shows that all soils have complex mineralogical compositions and are greatly affected by the particle size (Nenadović et al. 2010, Fonseca et al. 2012).

Although various non-destructive methods for evaluating soil microstructure exist, most of them do not provide sufficient information on the microstructure of collapsible soils. Therefore, there is a significant potential to apply X-ray Computed Tomography and Scanning Electron Microscopy imaging in the soil structure characterization of collapsible soils.

1.2   OBJECTIVES AND SCOPE

The main objective of this thesis was to develop a test procedure to investigate the microstructure of soils to aid in identifying potentially collapsible soils such as reworked residual granites of the Cape Granite Suite. Two potential non-destructive testing techniques in civil engineering were used as an alternate method to determine the microstructure.

Non-destructive and destructive testing programs were performed on representative soil samples, which comprised of reworked residual granites and residual Malmesbury shales. The residual Malmesbury shales were sampled and tested as a control for comparison in x-ray computed tomography and scanning electron microscope. The experimental program included collapse potential test, index tests such as particle size distribution, and microstructural evaluation using x-ray computed tomography (CT-Scan) and scanning electron microscopy (SEM).

Further objectives of this research study included the following:

I.   Perform the traditional geotechnical laboratory index tests to set a baseline for comparison.

II.   Configure the CT-scan and SEM of the Central Analytical Facility to execute scans on soil samples.

III.   Using CT-scanning and SEM as a form of test procedures to determine the microstructure of undisturbed samples of both reworked residual granite and residual Malmesbury shales.

IV.   Compare results from CT-scanning and SEM to the traditional geotechnical laboratory index test.

1.3   THESIS LAYOUT

The above-stated objectives were achieved by undertaking several activities, which are summed up in five chapters.

The background concepts of this study are described in Chapter 2. In addition, a general discussion of collapsible soils within South Africa is presented. It also elaborates on previous studies in soil microstructure characterization using both CT-Scanning and SEM. In addition, the benefits and shortcomings of each the methods are also discussed in this chapter.

Materials used and methods employed in achieving the aims of this study are discussed in Chapter 3. The methods are divided into two categories, namely traditional geotechnical laboratory tests and alternative tests (CT-scanning and SEM). The traditional geotechnical laboratory tests include the collapse potential test, which predicts the amount of settlement, aiding the researcher in understanding the collapse behavior. Avizo, VG Studio Max and ImageJ image processing software together with CT-Scan and SEM techniques are employed to determine the morphology and microstructure of the soils. Furthermore, multi-element analysis were also performed using SEM to know the effect of mineralogy on collapsibility. In addition, the sampling procedures and soil profiling method employed in the field work are explained. The local geology of the study area is provided in this chapter.

All test results, interpretation of these results along with discussions are presented in Chapter 4. The results from a CT-scan and SEM is compared to the traditional geotechnical laboratory index tests.

Chapter 5 includes a summary of all relevant findings, and conclusions with appropriate recommendations.

CHAPTER 2. LITERATURE STUDY

2.1   DEFINTIONS AND PROPERTIES OF COLLAPSIBLE SOILS

The ongoing debate and study of collapsible soils has resulted in several definitions by different investigators and authors. Below are a few of these definitions:

1. "..A soil which can withstand generally extensive stresses with little settlements at low in situ moisture content, yet showing a reduction in volume and associated extra settlement with no increase in the applied stress if wetting up occurs" (Schwartz, 1985).
2. "… A partially saturated soil that will exhibit additional settlement upon wetting, with no increase in vertical stress" (Jenning and Knight, 1975).
3. "… Any unsaturated soil that goes through a drastic particle rearrangement and an excessive loss of volume upon wetting with or without an imposed stress" (Dudley, 1970).

The above definitions suggest partially saturated soil as a critical component of collapsible soils. On the other hand, the best approach to examine, in detail, the properties of collapsible soils is to list the features commonly associated with it (Rogers, 1995). These include:

- An open soil structure;
- A high void ratio;
- A low dry density;
- A high porosity;
- Geologically young or recently altered deposit;
- High sensitivity and
- Low inter-particle bond strength

The first four features suggested by Rogers (1995) were selected as suitable descriptors for the term "microstructure" of collapsible soils. It should be noted that the focus of this thesis is on the microstructure of potentially collapsible soils.

2.2   COLLAPSIBLE GRAIN STRUCTURE

According to Schwartz, 1985, soils with a collapsible grain structure usually consist of a mixture of coarser soil particles cemented together by finer particles. The cementing materials include clays,

silts, and other colloidal material. Leaching of these materials results in a honeycomb-like structure (Koerner, 1984). The latter consist of voids into which the grains can rearrange when the shear strength is lost, thus resulting in a sudden reduction in soil volume (Schwartz, 1985).

2.3   OCCURANCE OF COLLAPSIBLE SOILS IN SOUTH AFRICA

The extensive investigation into the collapse phenomenon by Knight led to the conclusion of collapse occurring within Aeolian deposits. However, literature from Schwartz (1985) and Brink (1979) reports the occurrence of collapse settlement in a wide range of transported and residual soils. Examples are the settlement of the reinforced concrete columns of the water tower near White River in August, 1957, and the severe collapse settlement within the granites of the Basement Complex.

The above literature suggests that the distribution and occurrence of collapse settlement within transported and residual soils should be discussed separately.

2.3.1   Transported soils

If the products of weathering are transported by agents such as gravity, wind, water and glaciers and deposited in a different location, they constitute a transported soil (Craig, 2004). The definition indicates that the origin of transported soils determines its corresponding engineering problem (Jennings and Brink, 1978).

Table 2-1 The different types of transported soils and the possible engineering problems caused by each.

Transported Soil Type	Mode of Transportation	Source	Soil Type	Problems to Anticipate
Hillwash (Fine Colluvium)	Sheetwash	Acid crystalline rock	Clayey sand	Collapsible grain structure
		Arenaceous sedimentary rock	Sand	Collapsible grain structure
Gulleywash	Gulleywash	Local catchment	Gravel, sands, silts or clay	All possible problems
Aeolian Deposits	Wind	Usually mixed sources	Sand	Collapsible grain structure Compressibility
Littoral Deposits	Tidal waves	Usually mixed sources	Beach sand	Collapsible grain structure
Biotic Soils	Termites	Underlying soils	Often clayey or silty sand	Collapsible grain structure

Schwartz (1985) suggested the possibility of encountering these engineering problems within the transported soil types anywhere in South Africa.

2.3.2   Residual soil

Residual soils are that formed "in situ" by decomposition of the parent rock. Therefore, the degree of decomposition of residual soils determines its properties. Residual soils may be of igneous, metamorphic or sedimentary origin.

2.3.2.1   Residual granite

In South Africa the first reported case of collapse settlement of residual soils was associated with the Basement Complex residual granites, mainly as a result of the extensive foundation problems that have been encountered both in the Highveld and Lowveld of South Africa (Schwartz, 1985). Brink and Kantey (1961) identified collapse settlement within residual soils from three types of granites found in South Africa, namely: the Cape Granite Suite, the Archean granites and the Bushveld Complex granites.

In the humid eastern part of South Africa, the residual soils derived from the granites have a collapsible nature. These granites are associated with deep weathered soil profiles in these humid regions. During the weathering process, quartz remains unaltered, but feldspars are chemically altered due the interaction with water and carbon dioxide (Schwartz, 1985).

In regions of generally high precipitation, which is favorable for leaching, the colloidal kaolinite is to a great extent, removed in suspension by coursing groundwater resulting in the formation of soil with a collapsible fabric (Schwartz, 1985).

2.3.3   Other soil

A summary of the reported occurrence of residual soils with collapsible grain structure other than reworked residual granite, is presented in Table 2.2.

According to Schulze (1958), the reported occurrences of soils with a collapsible grain structure fall within or in close proximity to areas of annual water surplus. To support this literature, Schwartz (1985) laid emphasis on the fact that chemical decomposition and leaching played a major role in the formation of collapsible grain structures in residual soil.

Table 2-2: Summary of the reported occurrences of the collapse phenomenon in residual soils in South Africa, excluding granitic soils of the Basement Complex (Schwartz, 1985).

Stratigraphic Unit	Location	Soil Description Properties	Investigator	Remarks
Magaliesburg Quartzite Formation of the Pretoria Group of the Transvaal Sequence	Boschdal, south of Rustenburg	Moist reddish brown very loose intact micaceous silty medium and fine sand. Residual Magaliesburg Quartzite. Dry density 1585 kg/m^3	Brink	Collapse properties confirmed by oedometer tests. Decomposition in a favorable topographic situation produced highly leached residual soils. No indication of how widespread phenomenon may. Possible stratigraphic control, confining collapsible material to the stratum of highly feldpathic quartzite.

Table 2 2 "Continued"

Stratigraphic Unit	Location	Soil Description Properties	Investigator	Remarks
Rooiberg Group of the Bushveld Complex	Witbank	Thin layer (1.0) m of residual facet of low dry density (1430 kg/m^3)	Brink	No specific test carried out to evaluate collapse. Soil assumed to have collapse properties in the dry state because of low dry density.
Sibasa and Nzhelele Formation of the Soutpansberg Group.	Location not specified.	Deeply weathered residual basalt (clayey silt) dry density (1200 kg/m^3)	Brink	No specific test given to evaluate collapse. Indicated that soil has moderate collapse potential.

Cape granite suite	Near Stellenbosch and near Constantia.	Slightly gray mottled reddish brown stiff intact clayey silt. Residual Cape granite dry density (1440 kg/m^3)	Brink and Errera	Oedometer tests carried out on both sites to prove collapse properties.

Table 2 2 "Continued"

Stratigraphic Unit	Location	Soil Description Properties	Investigator	Remarks
Clarens and Elliot Formations and Ecca Group of the Karoo Sequence	Mainly central Transvaal	Residual feldspathic sandstone.	Weston and Brink	Tests carried out to prove properties of Ecca group and the Clarens sandstone
Diabase sill intrusive into shales of the Pretoria Group	West Rand	Dry orange loose clayey and sandy silt. Low dry density (1000 –1300 kg/m^3)	Wagener	Double oedometer tests showed residual diabase to have a heave /collapse behavior.

11

Berea red Sands residual from Quaternary calcarenites	Durban area	Red or orange silty sand.	Walsh Sparks and Errera	Laboratory tests carried out to prove collapse properties.

2.4   THE PROBLEMS ASSOCIATED WITH CONSTRUCTION ON SOILS WITH A COLLAPSIBLE FABRIC

Buildings, roads, pavements, airfields and other structures that have been constructed on collapsible soils may, upon recognition, function satisfactorily for years with or without any potential problems. However, there are many recorded and unrecorded problems associated with construction on soils with a collapsible fabric.

Taking into consideration the accumulated and vast knowledge gathered on these soils by several researchers, it appears reasonable to conclude that problems associated with construction occur due to one or more of the circumstances below (Schwartz, 1985):

1.   No geotechnical investigation was done;
2.   Execution of construction prior to identification of the collapse phenomenon. This is mostly the case with settlement and distortion occurring within many older structures (houses).
3.   Incorrect evaluation and identification of potentially collapsible soils during the investigation of the soil profile. Erroneous assessment of compressibility or bearing capacity as indicated by Jennings and Knights (1975) have been made due to the fact that a partially saturated condition will often yield a potentially collapsible soil with a dense or stiff consistency.
4.   Recommendations ignored by the client, contractor, or designer as proposed by the geotechnical engineer.

Presented below is a discussion of the problems associated with buildings, roads, and earth dams/reservoirs founded in soil with collapsible grain fabric.

2.4.1   Buildings

The unexpected permanent downward displacement of portions of the steel framed building near Witbank in 1955 brought to light the damaging effects of collapse settlement on the structures founded in these problematic soils (Schwartz, 1985).

Below are some factors leading to collapse settlement and causes of distortions of structures founded in soils with a collapsible fabric (Schwartz, 1985):

1. Collapse settlement may occur upon an increase in moisture content. If no ingress of water occurs, the performance and integrity of structures found in soils with collapsible fabric can remain unaltered for years, even for decades.

2. Collapse settlement of large magnitude (as high as 10 percent of the thickness of the potentially collapsible soil horizons) can occur beneath structures with evenly distributed loads.

3. Collapse settlement is often localized. For example, the foundation may settle as water infiltrates the ground from adjacent pipe leakages or areas with poor drainage due to ponding of rainfall. This causes unstable soils to collapse (collapsible soils). In addition, severe differential movement is induced, which is often equal to the total movement.

2.4.2 Roads, airfields, and railways

The first detailed report on failure of a road constructed on soils with collapsible fabric within South Africa occurred between Springs and Witbank. Knight and Dehlen, 1963, presented this during the third Regional Conference for Africa on Soil Mechanics and Foundation Engineering. According to both authors, densification or collapse in the in-situ subgrade resulted in a settlement of 150mm of the road surface. This was attributed to the increase in traffic loads resulting from coal haulage (Schwartz, 1985).

However, Schwartz's evaluation and conclusion from Knight and Dehlen reports was that an increase in moisture alone may not necessarily trigger collapse. Shear failure of bridging colloidal material caused by dynamic forces from traffic vibration is sufficient to initiate collapse.

2.4.3 Earth dams/reservoirs

Constructions of earth dams/reservoirs on soils with collapsible fabric are prone to general problems such as (Schwartz, 1985):

1. Settlement of the dam foundation due to excessive leakage from the stored water that saturates the foundation soil.

2. Improper compaction to break the bonds between soil particles causing severe damage to the embankment foundation or total failure of the embankment itself.

3. Materials for the reservoir embankment construction are excavated from the planned storage area. In a soil profile which includes potentially collapsible soils, shortage of material may be experienced. This is because the soil particles are re-arranged in a denser state which is caused by compaction volume reductions.

2.5 EVALUATION AND PREDICTION OF COLLAPSIBLE SOILS

The first step in identifying a potential collapsible soil is from a comprehensive field observation. In order to quantify the extent of collapse, laboratory tests or in-situ testing are engaged. Comprehensive field observation, laboratory tests, and in-situ tests, coupled with collapse predictive models is used to evaluate collapsible soils (Basma et al. 1993).

2.5.1 Field identification

Comprehensive field observation and correct recording of the soil profile is the prime factor in determination of soils with a collapsible fabric.

Dry or marginally soggy soils show partial saturation and despite the fact that the in-situ consistency will rely upon the moisture content, a free or open fabric will typically be obvious while recording the soil profile. In addition, visualization and recognition of colloidal coatings and clay bridges are enhanced by using a hand lens. Moreover, the origin of soil within a profile (if accurately identified) will also aid the prediction of collapse (Schwartz, 1985).

A simple sausage test as described by Jennings and Knight (1975), is another form of field identification. Two undisturbed cylindrical samples of the same volume are cut from the soil. One of the two samples is then wetted and moulded to structure a chamber with the height of the first sample. When compared to the original, a decrease in length will give an indication of a collapsible grain structure.

In addition, structural damages such as cracking and distortion of existing buildings in urbanized areas are important field identifications. Furthermore, concrete structures will tilt towards the region of maximum collapse. Similarities in the cracking pattern are normally linked to the collapse and heave phenomenon (Schwartz, 1985).

2.5.2   Laboratory index test

Generally, problems with collapse are linked to silty or sandy soils with low clay content. Particle size distribution and Atterberg limits will aid in recognizing soils with collapse behavior. However, it is important to note that low clay content within a soil matrix does not always imply the future occurrence of collapse settlement. A physical property such as a low dry density is normally exhibited by soils with a collapsible fabric. On the contrary, it is important to take into consideration that not all soils with low dry densities will collapse.

Taking into consideration the extensive variety of soils which show collapse properties, it is obvious that these tests ought to be viewed merely as index tests, which may help with the identification of potentially collapsible soils and possibly the depth to which these soils occur within the soil profile.

The collapse potential test is an index text carried out using an oedometer apparatus, specifically the single consolidometer test. In a single consolidometer test, an undisturbed sample is loaded into the oedometer ring, and a consolidation test is carried out with the sample at its natural moisture content with loads applied incrementally up to 200 kPa. The sample is saturated at 200 kPa (Schwartz, 1985). A typical collapse test result is shown in Figure 2.1.

The collapse potential is not a design parameter, but instead an indicator test to guide the investigator with regards to the collapse situation and to indicate whether there is the need for further investigations (Jennings and knight, 1975). Interpretation of the severity of collapse is based on the guiding values of collapse potential given by Jennings and Knight. These are listed in Table 2.3.

16
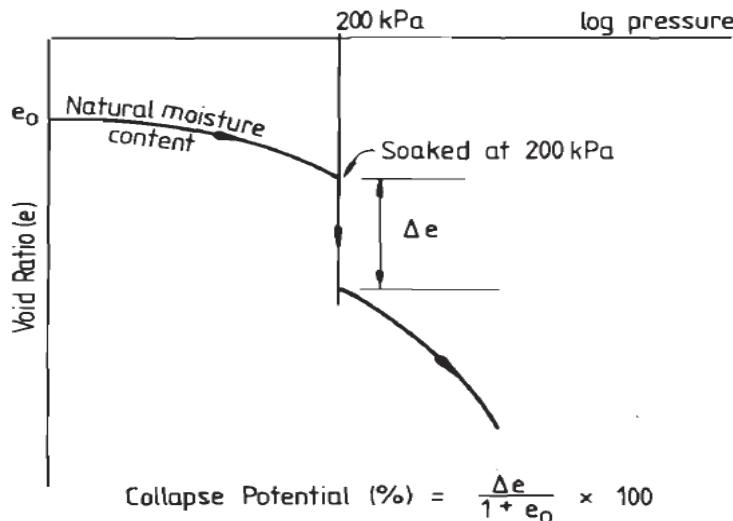
Figure 2-1: A typical collapse potential test result after Schwartz (1985).

Mathematically, the collapse potential, Cp, according Schwartz (1985) may be calculated as:

$$CP = \Delta \varepsilon = \frac{(e_1 - e_2)}{(1 + e_0)}$$

Where e_0 = natural void ratio of the soil, and $\Delta \varepsilon$ = vertical strain

Table 2-3: Collapse potential guiding values by Jennings and Knights, 1975 (modified after Schwartz, 1985)

Collapse Potential	Severity of Problem
0% - 1%	No problem
1% - 5%	A Moderate problem
5% - 10%	Problem
10% - 20%	Severe problem
>20%	Very severe problem

17

2.6   OTHER METHODS OF IDENTIFICATION OF COLLAPSIBLE S SOILS

Several methods for evaluating the physical parameters for collapsible soil identification are available in literature as shown in Table 2.4.

Table 2-4: Existing criteria for predicting soil collapsibility (modified after Ayadat and Hannah, 2012).

Expression	Investigator	Remarks
$K = \dfrac{e_L}{e_0}$	Denisov	$K = 0.5\text{-}0.75$ highly collapsible $K = 1.0$ non collapsible loams $K = 1.5 - 2.0$ non collapsible soils
$W_L / \left(\dfrac{\gamma_w}{\gamma_d} - \dfrac{1}{G_s} \right)$	Gibbs and Bara	< 1.0 collapse occurs
$\alpha = (e_0 - e_L)/(1 + e_0)$	Markin	$\alpha > -0.3$ prone to swelling $\alpha > -0.1$ and $S_0 < 60\%$, susceptible to collapse
$\alpha = (e_0 - e_L)/(1 + e_0)$	Minheev	$S_0 < 0.6$ and $\alpha > -0.1$ susceptible to collapse (this criterion is known as the new soviet building code)
$K_d = W_L - W_0/ I_p$	Priklonskij	$K_d < 0$ highly collapsible soils, $K_d > 0.5$ non collapsible soils, $K_d > 1.0$ swelling soils

18

Expression	Investigator	Remarks
$K_L = \left(\frac{W_0}{S_0} - W_P\right)/I_p$	Freda	For $S_0 < 60\%$ $K_L > 0.85$ collapsible soils
$R = \frac{W_S}{W_L} = \left(\frac{\gamma_w}{\gamma_d} - \frac{1}{G_s}\right)/W_L$	Gibbs	$R \geq 1\%$ collapse susceptible. This was also put into graph form
$\alpha = \acute{y}_{0d}/\acute{y}_{Ld}$	Markin	$\alpha > 1.3$ prone to swelling $\alpha > 1.1$ prone to collapse
$\acute{y}_{0d} < 1.28$ g/cm^3 , $\acute{y}_{0d} > 1.44$ g/cm^3	Clevenger	Settlement will be large, Settlement will be small
$R = 5.5 - 3.82\log(W_L/W_P) - 1.63\log W_P - 1.24\log C_U - 0.918\log P_{10} - 0.303 P_{200} + 0.465\log\left(\frac{D_{60}}{D_{40}}\right) - 0.45\log\left(\frac{D_{99}}{D_{50}}\right)$	Anderson	

From Table 2.4 above, it is noticeable that all the investigators' research revolved around void ratio, the relationships between density and water content, between water content and Atterberg limits, and between density and Atterberg limits, and methods based on particle size distribution (Ayadat & Hanna 2012). However, the first four of the common features of collapsible soils, as suggested by Rogers (1995), determines the volume reduction and structural stability of the soil and thus there is the need to investigate the microstructure of the collapsible soils.

2.7   COMMON METHODS USED FOR DETERMINATION OF SOIL MICROSTRUCTURE

The microstructures of a soil comprise the particle morphology, porosity, particle size, pore size, void ratio and the mineral composition. These properties are determined by using different methods. The accuracy of these methods depends on the type of sample, the device availability, the sample preparation method, analysis time, and cost.

2.8   METHODS OF PARTICLE SIZE ANALYSIS

The methods for determining the particle size is broadly categorized into three groups namely: Separation methods, counting methods and ensemble methods. The effectiveness and accuracy of the separation methods depend on the applied force for separation of particle size. Examples of the separation method include sieving, sedimentation, disc centrifuge, capillary hydrodynamic fractionation, and sedimentation field flow fractionation.

2.8.1   Sieving

Sieving has been utilized as a simple method to measure and classify particles according to their distribution for a considerable length of time. The sieving process can be done either wet or dry, and each of these two methods has its own advantages and limitations.

The sieving process involves stacking a pile of sieves with the aperture size decreasing from the top to the bottom. Regardless of the standard sieve used (ASTM and/or THM1), for a coarse material, particle sizes extending to one hundred and fifty microns will yield a reliable particle size distribution. On the other hand, particle size distribution of finer material (less than one hundred and fifty microns) when using dry sieving will yield significantly less accurate results. This can be attributed to the fact that, in sieve analysis, particles are assumed spherical and this is not true for all particles. In addition, needle or rod like particles will either pass through the sieve or remain behind on the sieve, depending on its orientation. This alters the integrity of the mass-based results.

2.8.2   Sedimentation

Sedimentation is the process by which solid particle settles from suspension in a fluid media at different velocities. Larger particles settle faster than finer particles. Sedimentation is carried out

either by hydrometer or pipette and, coupled with sieving, has been used in the quantitative analysis of particle size distribution. This is an accepted as standard practice in most industries worldwide.

Although hydrometer sedimentation or the pipette method has many inherent errors, it is popular for its simplicity and cost (Conley, 1969). The effect of Brownian motion on sedimentation methods for particles less than one micron (1µm) yields unreliable results of sedimentation analysis. They also require a large amount of sample for particles less than two microns (2µm) i.e. 50g for the hydrometer method and 20g for the pipette method (Di Stefano et al. 2010).

The governing principle of the hydrometer sedimentation analysis is derived from Stokes' equation; an expression describing the velocity at which particles moving through a fluid medium settles in suspension. Innate in Stokes' law are the assumptions that: 1) particles are smooth, rigid and spherical particles, 2) there is unrestricted fall, 3) there is laminar medium flow and 4) body diameter is the diameter of a sphere. Stokes' first assumption contradicts the fact that most soil particles are non-spherical such as silts and clay which are irregular and platty in shape.

2.9   ENSEMBLE METHODS

For the ensemble methods, data for different particle sizes within a sample are captured at the same time by light, electron or x-ray emission and the data are processed to produce a particle size distribution. Common techniques include laser diffraction, x-ray computed tomography and scanning electron microscopy. Detailed explanations on x-ray computed tomography (CT-scan) and scanning electron microscopy are given in section 2.16 of this thesis.

2.9.1   Laser Diffraction

The optical properties of a particle are the controlling factor in particle size analysis by laser diffraction. In laser diffraction, particle size is calculated from the collection of light intensity data by a detector. The passage of the laser beam is through the sample particle at many different angles from the axis of the laser beam, as depicted in Figure 2.2. Fraunhofer diffraction and Mie theory of light scattering are the common diffraction theories used in particle size analysis by laser diffraction. Both theories claim that "the particle dimension is the optical spherical diameter"(Di Stefano et al. 2010).

Although laser diffraction is widely used due to its simplicity and the capability of measuring a wide range of particle sizes (with the smallest particle limit as 1µm and the largest particle limit as 600µm). Kowalenko & Babuin (2013) and Di Stefano et al. (2010) argued that the technique has some inherent factors limiting its performance. Kowalenko & Babuin (2013) concluded from their research conducted on five different types of soils with a wide range of textures, that for a given weight of sample, the sample's distribution becomes too large to employ the use of the modern laser diffraction instrumentation for particle size analysis as the change in particle geometry decreases. To support this argument, Burma et al. (1997) proposed that another limitation in the laser soil particle sizing is the accuracy of the optical parameters available for soil particles. This limitation leads to the under-estimation of clay particles sizes, although studies conducted using laser particle sizing produce repeatable results.
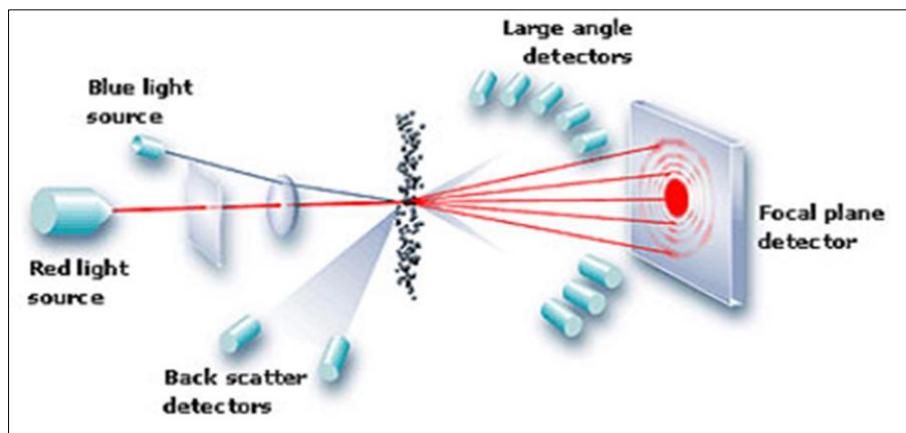
Figure 2-2: Principle of a laser diffraction (copyright Malvern Instruments Ltd)

2.10   METHODS OF PORE AND PORE DISTRIBUTION ANALYSIS

Soil porosity is the measurement of voids between the soils particles or grains. The porosity and the pore size distribution are a function of the pore geometry, directly affected by the packing density, particle size, particle shape, and cementation.

Porosity and pore size distribution is gaining prominence in microstructural studies of soils due to its effect on the engineering properties of soils such as collapse and swelling. Several studies have been conducted to quantify porosity and pore size distribution of different materials such as soil, cement, wood and metals using techniques including water retention curves, mercury intrusion porosimetry, tomography, nitrogen adsorption, and microscopy, but all these techniques have their

limitations (Abell et al. 1999; Nimmo 2004; Romero & Simms 2009). However, to determine the geometric properties of pores, Abell et al. (1999); Nimmo (2004), and Romero & Simms (2009), suggested the application of image analysis using microscopes and tomography.

2.10.1 Mercury Intrusion Porosimetry

Mercury intrusion porosimetry (MIP), like the water-retention based technique, is a widely used method for pore and pore distribution measurement but uses air as the fluid medium.

The MIP technique involves the injection of a non-wetting (mercury) fluid at high pressure into the pores of a dry soil. The mercury intrusion is done incrementally at a contact angle greater than 90°. A derived relationship between the external pressure (mercury) and the mercury content coupled with an appropriate surface tension value will yield the pore size distribution estimation (Nimmo 2004; Abell et al. 1999).

This method is fast and simple, but has several limitations (Nimmo 2004; Abell et al. 1999; Romero & Simms 2009) such as:

- The assumption that pores within a soil is regular geometrically
- Sample preparation requires the removal of water
- Constricted porosity
- Restricted porosity
- Undetected porosity

In summary, Nimmo (2004); Abell et al. (1999), and Romero & Simms (2009) states that MIP should be coupled with an image analysis to establish a better understanding of porosity and pore distribution.

2.10.2 Gas Adsorption Isotherm

Gas adsorption has played a major role in pore structure analysis globally. Nitrogen gas has remained universally for gas adsorption techniques, but other researchers (Hajnos et al. 2006; Sing, 2001) alternatively explore other non-corrosive gases such as carbon dioxide and argon.

The nitrogen adsorption isotherm is based on the theory of Brunauer–Emmett–Teller (BET) which states that the determination of the specific surface area of materials is based on the model of monolayer-multilayer adsorption (gas molecule on a solid surface) at 77 Kelvin (K). Although this technique is widely accepted, a recent study by Sing (2001) pinpointed the inability of the technique to analyze structural correlations between pores (pore shape, surface roughness, and fractal dimensioning). Hajnos et al. (2006) and Okolo et al. (2015) supported the argument that the complexity of pore characterization is inconclusive without the use of 3D images (CT-Scan, SEM) and the other experimental techniques. However, a research conducted by Sing (2001), suggested that nitrogen adsorption should be regarded as a first phase for pore analysis of highly porous materials.

2.11   SOIL MINERAL COMPOSITION ANALYSIS

The mineralogy of a soil plays a major role in processes such as soil erodability, expansiveness, and collapsibility. The identification of soil mineral constituents is dependent upon the availability of the technique required (for example x-ray fluorescence spectrometry, SEM, CT-scanning) and experience of the researcher (soils scientist or geologist). Some of the basic methods for determining the soil mineral composition include differential thermal analysis, infrared analysis, and chemical analysis. The most recent of the laboratory based techniques include x-ray diffraction and x-ray fluorescence spectrometry which, according to Gerhart et al. (2004), are most suitable for mineral identification and also yields reliable results.

However, Kalnicky et al. (2001) and Imanish et al. (2010) refute the reliability of x-ray fluorescence spectrometry. According to these authors limitations such as depth of x-ray penetration, water content in the soil and matrix effect has a negative influence on the performance and the reliability of the x-ray fluorescence spectrometry results. This argument was supported by Argyranki et al. (1997); VanCott et al. (1999), and Johnson et al. (1995). They state that the largest influence on the accuracy of XRF analysis and results is soil heterogeneity which is highly dependent on the grain size.

To avoid this limitation Woodward & Amjad, (n.d.) and Illinois, (n.d) suggested scanning electron microscopy with energy dispersive x-rays as an effective and most reliable technique to determine soil mineralogy.

2.12   BACKGROUND CONCEPTS

The primary objective of this study is to develop alternate geotechnical test methods for measuring the microstructure of potential collapsible soils using the CT- scanning and SEM at the Central Analytical Facility of Stellenbosch University. These methods are greatly used in the medical field, but its application in the civil engineering industry is still being evaluated. This section explains the various concepts related to the development of the geotechnical test methods for investigating microstructure of soils using a CT-scanning and SEM. These concepts were based on information gathered from medical radiography, image processing and soil physics to determine the porosity, void ratio, particle size and particle shape, pore size distribution and mineralogy of potentially collapsible soils.

2.13   X-RAY COMPUTED TOMOGRAPHY

CT scanning involves the visualization of the internal structure of objects without sacrificing it. CT scanning has been used in the medical field for several decades, but because of technological advancement, its usage is continuously growing as an analytical tool in the civil engineering industry. Although there is a difference in the conventional medical CT and industrial CT (e.g. Micro CT); the technical principles are the same for the two. Data acquisition and image reconstruction are the two major processes that engulf CT scanning. Image reconstruction is the conversion of the measured x-ray computed tomography signals to a two-dimensional (2D) or three-dimensional (3D) image. Various mathematical procedures are employed (e.g., "Filtered back projection," the "Feldkamp algorithm," or Fourier-transform methods) depending on the technique and instrument used. Each process is explained in detail in the following paragraphs.

2.14   THEORY OF X-RAY SCIENCE

The exposure of a sample to x-ray beams involves the scanning of the specimen, thus taking photographs of the sample from multiple angles. An x-ray involves the penetration of various materials using the ability of electromagnetic radiation (high-energy photons). When an x-ray beam is directed to a material, part of their energy is either scattered, absorbed, or will travel through the material without any interaction with the material particles (Russ, 2002).

The thickness, density, and atomic number of the material, coupled with the energy of the photons, greatly affect the amount of x-ray transmitted, as shown in the Figure 2.3 below. For example, a dense object (e.g. metal and rock) absorbs more rays than less dense materials such as plastics.

The purpose of radiography is to obtain a detailed image of the internal structure of an object. Radiography requires careful control of a number of different variables. A single image is not sufficient to give a description of an object's internal structure.
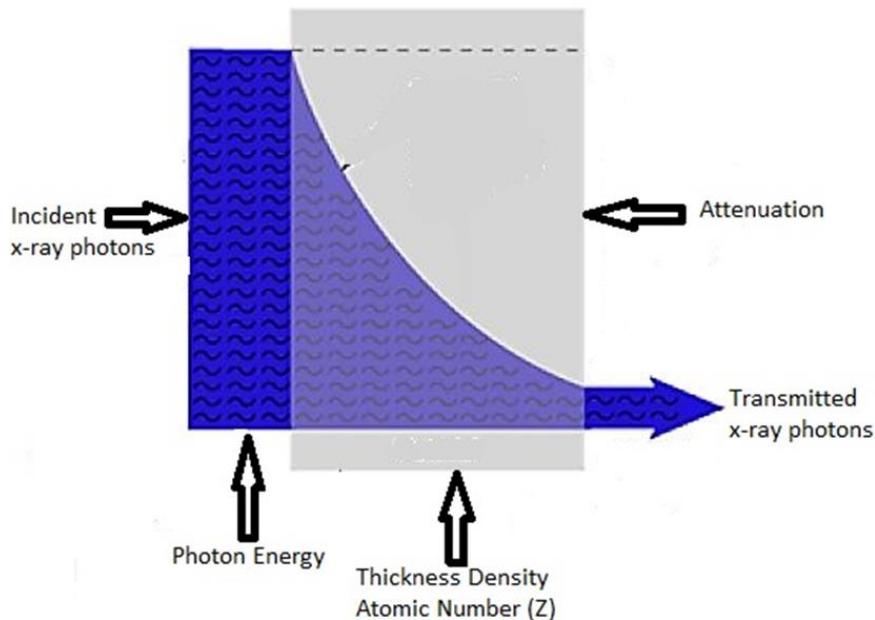
Figure 2-3: Factors affecting the transmission of x-ray through a material (modified after Sprawls, P. 1995).

2.15   CT-SCAN DATA COLLECTION

Data collection generally occurs after the visualization of an object image file, which is visualized and analyzed using a wide variety of 2D and 3D-based image rendering software.

The CT data collection is dependent upon a number of variables, which includes; the number of views and the signal acquisition time per view. To capture a view, scanning can be done either by half rotation (180°) or full rotation (360°) at a closely or widely spaced view. A more closely spaced view yields finer image resolution and vice versa (Russ, 2002). The Electric Phoenix

26

VTomeX L240 / NF180 scanner of the University of Stellenbosch acquires approximately two thousand (2000) views (images) for a full rotation (360°) image acquisition time of five hundred millisecond (500ms) per view (image). The scan duration is dependent on the degree increment and the camera exposure time, which is directly affected by the sample density. Reconstruction is carried out after the last x-ray image is captured.

2.15.1 Image reconstruction

Reconstructed images are processed from data as a series of angular projection images, which are displayed on computer monitors as a graphical representation of an object. This involves the conversion of sinograms into two-dimensional images sliced by mathematical procedures of the original image. A reconstructed image can be formed by using the Shepp-Logan phantom as an original image. This is achieved by deciding on the number of projected angles between the rays with respect to the scan location (Shepp and Logan, 1974). The user determines the number of project angles. A collection of stacked sections of the various projections at several angles is termed sinogram and it is always linear to the original image. Figure 2.4 depicts an original image (Shepp-Logan phantom) and its Radon transform, often known as its sinogram.
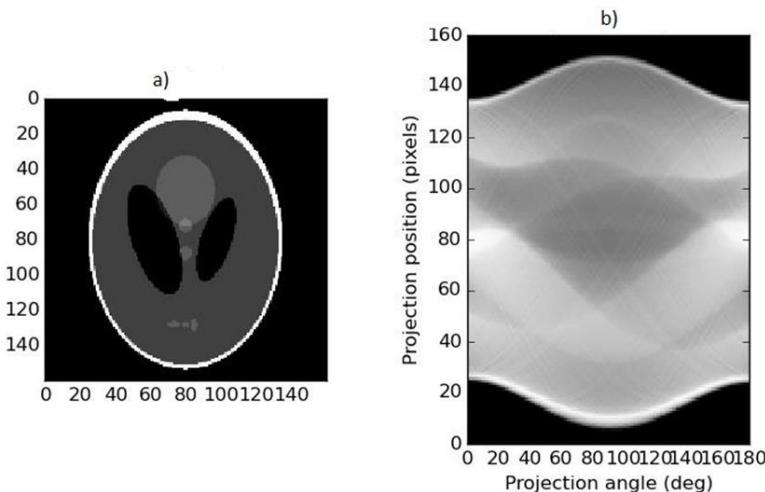
Figure 2-4: A Shepp-Logan Phantom and reconstructed Image (Sinogram). (a) Original image; (b) radon transforms (modified after Shepp and Logan, 1974).

27

Most commonly used image reconstruction techniques include back-projection (Ramachandran and Lakshminarayanan, 1970), and Shepp and Logan phantom filter (Shepp and Logan, 1974). In the medical sector, the Shepp and Logan filter is used for noise correction.

The data intensity in a sinogram during image reconstruction is converted to CT values (numbers). These values are determined on a scale of 12-bit, which yields approximately four thousand and ninety-six (4 096) values and 16-bit for which sixty-five thousand five hundred and thirty-five (65 535) values are possible. Modern industrial CT scanners use a 16-bit scale starting from zero (0).

2.16   ELECTRON MICROSCOPY

Microscopy has become a common tool in geology, geochemistry, as well as material science for microstructural studies (Lin & Cerato 2014). Although sampling techniques and sample preparation are time consuming and tedious, the morphology and mineral composition of individual particles can easily be measured, thus making microscopy a widely utilized technique. The results from a microscopic analysis are dependent upon the accuracy of the statistical factors, sample preparation, and the sampling techniques. The user should know this prior to using the technique.

2.17   SCANNING ELECTRON MICROSCOPY

Optical microscopes, although with limited resolution, is the simplest and most affordable method for material characterization (Brundle, 1992). Images produced under optical microscopes have resolutions of one to two micrometers by visible lights having a wavelength ranging from four hundred nanometers (400nm) to seven hundred nanometers (700nm). This applies to most optical microscopes (Brundle, 1992). Scanning electron microscopy (SEM) operates on optical principles, but with electrons instead of light with magnification over 10 000 times. Unlike any other optical microscope, SEM generates images using electrons within a short time and at high accuracy. According to Bindle, (1992), resolution of SEM produces a standard energy of about 5 kiloelectron volts (keV).

As a result of its higher resolution and magnification power, SEM has been deployed in the investigation of soil microstructure (Remley 1989; Sullivan 1990; Polish 1995; Millogo et al. 2011). A microstructure ranging from several millimeters to hundreds of nanometers has been determined

successfully (Nenadović et al. 2010), yet, it has some primary limitations such as sample preparation, lens aberration, and long analytical time.

According to Trzcinski (2004), sample sizes for SEM analysis, though making up a very small (about one square centimeter) area of the mount provides a wider range of enlarged images for analysis. Franck & Herbarth (2002), concluded from their research on "Using Scanning Electron Microscopy for Statistical Characterization of the Diameter and Shape of Airborne Particles at an Urban Location" that electron microscopy provides additional information such as shape factor distribution, which cannot be determined by other soil microstructural methods such as laser diffraction, sieving, and sedimentation.

2.18   CONSTRUCTION OF SCANNING ELECTRON MICROSCOPY

The Zeiss EVO MA 15 used in this study allows for viewing dry samples by operating at either a high or low vacuum. The accelerating voltages of the available microscopes range between 0.2 and 30kV and the magnification ranges from seven (7x) to one million (1 000 000x) times. The stage can move 125 x 125x 60mm in the X, Y, and Z directions, making it possible for samples up to a height of 100mm and diameter 200mm to be viewed.

There are several accepted diameters utilized in microscopy to estimate the diameters of the two dimensional images, and particles viewed under the microscope as illustrated in Figure 2.4. Listed below is the accepted diameters (Allen, 1975):

1. Martin's diameter (M) is the length of the line which bisects the image of the particle. The lines may be drawn in any direction which must be remain constant for all the image measurements.
2. Feret's diameter (F) is the distance between two tangents on opposite sides of the particle, parallel to some fixed direction.
3. Longest diameter. A measured diameter equal to the maximum value of Feret's diameter.
4. Maximum chord. A diameter equal to the maximum length of a line parallel to some fixed direction and limited by the contour of the particle.
5. Perimeter diameter. The diameter of a circle having the same circumference as the perimeter of the particle.

6. The projected area diameter (da) is the diameter of a circle having the same area as the particle viewed normally to a plane surface on which the particle is at rest in a stable position.

2.19   PRINCIPLES OF SCANNING ELECTRON MICROSCOPY

In SEM, electron –sample interaction produce five types of signals. The kinetic energies carried by the emitted electrons generate these signals. These signals include the backscattered electrons, secondary electrons, diffracted backscattered electrons, photons, light, and heat.

SEM analysis revolves around the production of sample images, structure, and orientation of individual particles within a sample and composition of multi-phase samples using the secondary electrons diffracted backscattered electrons and the backscattered electrons (Goldstein, J. 2003). This is shown in Figure 2.5.

X-ray tubes produce X-ray photons by accelerating incident electrons colliding with electrons within the orbits of the atoms in the sample producing charged photons. Some of these photons have sufficient energy to eject an electron, which is bound to the nucleus of the atom. When an inner orbital electron is ejected from an atom, an electron from a higher energy orbital will be transferred to the lower energy orbital. This produces x-ray radiations for the individual elements within the sample from the electron beam (Goldstein, J. 2003).

SEM analysis is considered as non-destructive; because the mechanical or physical properties of the sample being investigated, is not altered by the x-rays emitted by the electrons. The same material can therefore be used again.
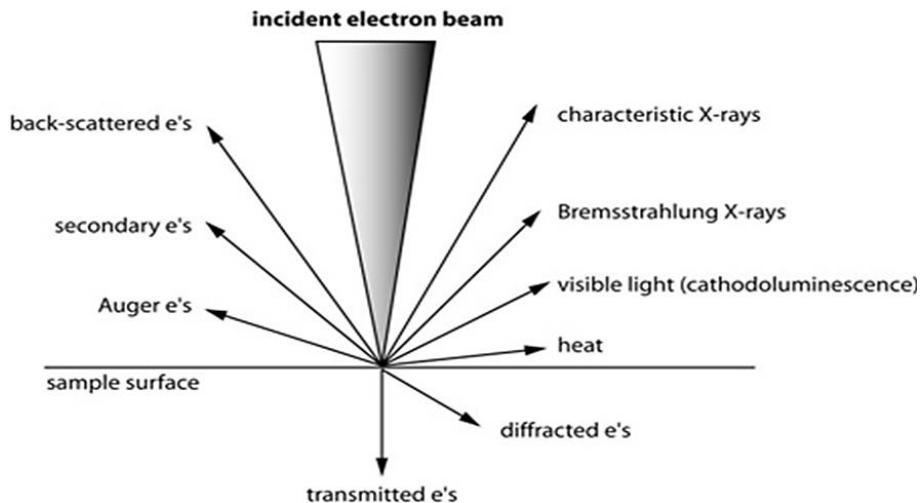
Figure 2-5: Various types of signals between electrons and sample interaction (Darrell Henry, Louisiana State University, unpublished)

2.20   BASIC CONCEPTS OF IMAGE ANALYSIS IN SCANNING ELECTRON MICROSCOPY

Image processing in microscopy is the most important factor in determining soil particle morphology. The process involves the use of digital images and image processing computer software. A flowchart in Figure 2.6 shows the different processes involved in image analysis using SEM.
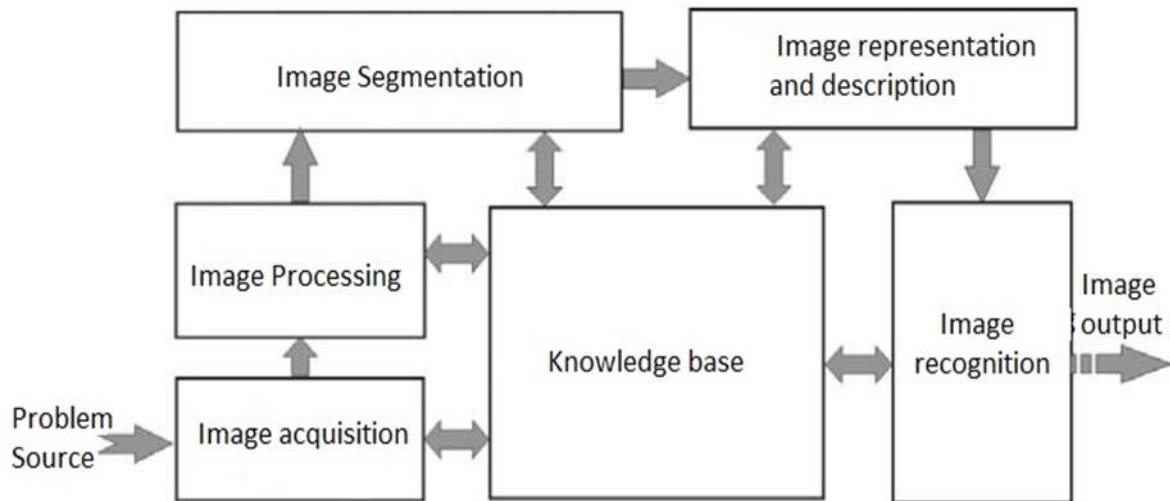
Figure 2.6: Flowchart for image analysis (modified after Gonzalez, 1993).

31

2.20.1 Image acquisition

The first step of microstructural examination using SEM is imaging. Imaging of samples by SEM produces higher accuracy. The mapping process produces image acquisition in SEM. The mapping process involves the transformation of specimen space to CRT space and this can be done in two ways; which includes line scanning and area scanning (Goldstein, J. 2003). Line scanning and area scanning are the processes involved in the mapping process (Goldstein, J. 2003). Images are acquired pixel by pixel and line by line at a slow rate in order to obtain an image of better quality which is stored on a computer hard drive and processed at a later stage (Goodhew et al. 2001).

2.20.2 Image processing

Image processing is the modification of varying electrical signals produced from the detector during image acquisition. The natural contrast available for specimens will occasionally be found as being too weak or too strong thus decreasing their visibility. These limitations are rectified by a variety of signal processing techniques which are available for SEM (Goldstein, J. 2003). The basic signal processing techniques include contrast control, brightness control and gamma control (Goodhew et al. 2001). For particle analysis, the signal processing method commonly used is the gray level of the image.

2.21   IMAGE SEGMENTATION

Segmentation is the separations of a digital image into sets of pixels which is a vital step in determining particle and grain boundaries in a particle image. The accuracy and reliability of a particle area are dependent on the segmentation process.

Domain segmentation problems have led to the development of several image segmentation algorithms and techniques. These techniques and algorithms are broadly categorized into a semi-interactive approach and fully automatic approach (Khan 2013). Thresholding is one of the simplest and most widely used intensity based image segmentation techniques, although there are other commonly used methods such as discontinuity based segmentation and region based segmentation (including region growing, region splitting and region merging), (Khan, 2013).

2.21.1 Intensity based segmentation

Threshold based technique is an intensity based segmentation approach. In threshold approach, an image is partitioned into two classes of pixels. The first range of pixels, consists of a bright foreground and the other range of pixels make up the dark background. Thresholding of intensity based segmentation can be implemented in the following ways: 1) globally using the appropriate thresholding, T 2) Variable thresholding, if T can change over the image 3) Local or regional thresholding, if T depends on a neighborhood of (x, y) and 4) adaptive thresholding, if T is a function of (x, y). This is represented in the equation below (Nagabhushana 2005):

$$g\ (\text{x, y}) = \begin{cases} 1 & for \ \ i(x,y) \geq T \\ 0 & for \ \ i(x,y) < T \end{cases}$$

Where g (x, y) is the output image

i (x, y) is the input image, and T the Threshold

The results of a thresholding technique employed in image segmentation depend on the threshold value applied, which is also dependent on the method of detecting the threshold value. Examples of the methods for threshold value detection are bimodal histogram, p-tile thresholding, and optimal thresholding, but the most commonly used is Otsu's histogram based method although with minor modification by several researchers (Nagabhushana 2005).

The Otsu's method is a straightforward automatic threshold selection procedure. Moreover, its application is very simple and applicable to other methods such as the multi-thresholding and bimodal thresholding method with its validity supported by several experimental results (Smith et al., 1979).

2.21.2 Discontinuity based segmentation

Point detection, line detection and edge detection are the three approaches in determining the abrupt increase or decrease in gray level intensity of a digital image (Khan, 2013).

Point detection involves the separation of an isolated point with a distinct gray level intensity from its background, as shown in Figure 2.7. This occurs when the gray level of the isolated point is above a set threshold.
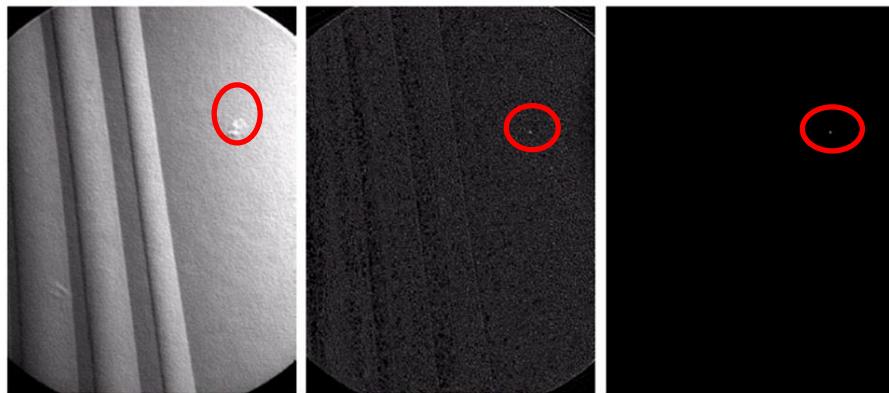
Figure 2-6: Illustration of Point Detection (image extracted from www.slideshare.net), a)X-ray image, b)Results of point detection, and c)Results of threshold.

On the other hand, a digital image may consist of thick line pixels running at different but definite orientations (vertically, horizontally, or obliquely inclined). In order to extract these lines; a line detection method is used (Thakur & Madaan 2014).

Edge detection is applied to distinguish the boundaries between two regions within an image. These boundaries or edges consist of a set of connected pixels that lie within the two regions based on the rapid changes in the intensity levels.

An image may consist of a step-edge, ramp edge, roof edge or ridge edge. These are further categorized into two sets of models, namely: Model of the ideal digital edge and model of ramp digital edge (Thompson et al., 1981). This is shown in Figure 2.8.
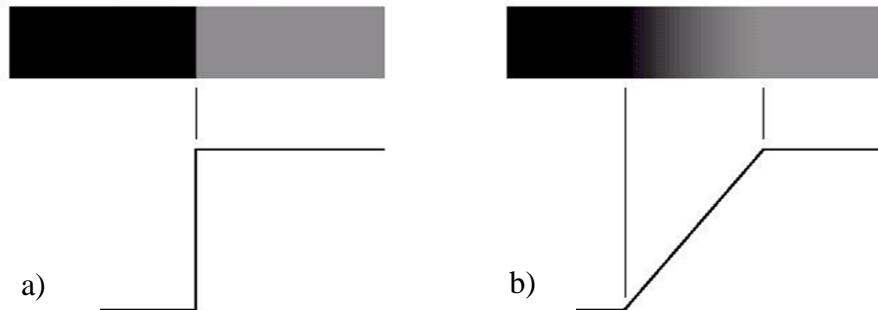
Figure 2-7: The two models of edge detection (modified after Thompson et. al, 1981), a)Model of an ideal digital edge and b)Model of a ramp digital edge.

2.21.3 Region based segmentation

The region based technique is categorized into two methods, namely: the region growing method, and the region splitting and region merging method. The region based method starts with a reference point also known as the "seed point." With the aim of producing a homogenous region of similar characteristics, seed points are added one by one, but do not include dissimilar pixels in another region. The results obtained from the process is termed region growth.

The shape, texture, color, and gray level of neighboring pixels are checked during image segmentation using the region-based method. This is termed the similarity check. The outcome of the latter is either positive or negative. A positive outcome implies region growth whilst negative implies a similarity check failure.

Region splitting and region merging are post-processing methods employed after segmentation. The process involves the separation of homogeneous regions with similar properties into quadrants based on a well-defined criterion. Splitting and merging is repeated if the outcome of the first quadrant is negative; until the set criteria are satisfied (Khan, 2013). This is shown in Figure 2.8.

35
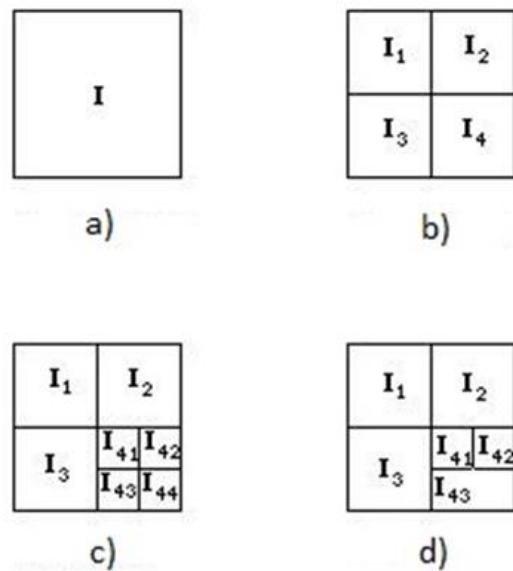
Figure 2-8: The region splitting and region merging process. (a) Original image; (b) first split; (c) second split; (d) Merge (image extracted from www.cs.cf.ac.uk/Dave/Vision_lecture/node34

CHAPTER 3. MATERIALS AND METHODS

3.1   INTRODUCTION

CT scanning and scanning electron microscopy procedures developed in this thesis were used to quantify the morphology (shape, sphericity and roundness), porosity, grain size distribution and pores size distribution of reworked residual granites and residual Malmesbury shale. The results of these measured parameters were compared to the results of traditional geotechnical index tests to determine grain size distribution. Each of these index tests was performed in accordance with American Society for Testing and Materials (ASTM) standards. This chapter deals with the experimental methods applied in this research.

3.2   GEOTECHNICAL LABORATORY TESTS

Mechanical sieving, hydrometer analysis, collapse potential tests and the standard laboratory methods to determine the Atterberg limits were carried out and used for the experiments. These methods were used to describe the physical nature and state of the soil samples and also to separate the soils into classes or groups. The soil description and classification was done in accordance with the ASTM standards. Table 3.1 gives a summary of the various index tests performed.

Table 3-1: Summary of the number of Geotechnical laboratory index tests performed.

Index Test Type	Number of Tests Performed	Mass of soil used (g)	Remarks
Atterberg Limits	6	100g of soil from each pit	
Sieving	6	500g of soil from each pit	

Index Test Type	Number of Tests Performed	Mass of soil used (g)	Remarks
Hydrometer Analysis	8	50g of soil from each pit	Test for Ernie Els Wines pit 1 and Boland Bricks pit 3 was repeated due to high temperature.
Collapse Potential	15	N/A	Two of the specimens were used as a trial test to study the effect of load shedding during test . One specimen was damaged.

3.2.1   Atterberg limits

This comprises the liquid limit, plastic limit and plasticity index which can be determined by standard laboratory methods. These tests were performed to assist with classification of the soils in question and was performed in accordance with ASTM D4318-95A

The engineering properties of fine grained soils are greatly affected by the water content. It was thus deemed necessary to clarify these effects by determining the Atterberg limits. By varying the amount of water, a soil may appear in four states namely: Solid state, semisolid state, plastic state, and liquid state as shown in Figure 3.2. When a soil is in the plastic state it is easily remoulded and can thus be deformed beyond recovery with no change in volume. The liquid limit (LL) is the upper limit of water content at which a soil is in the plastic state. The liquid limit is defined as the water content at which 25 blows are required to close the bottom of a 13mm wide groove in the soil. The Casagrande apparatus was used to determine the LL (Craig, 2004). See Figure 3.1.
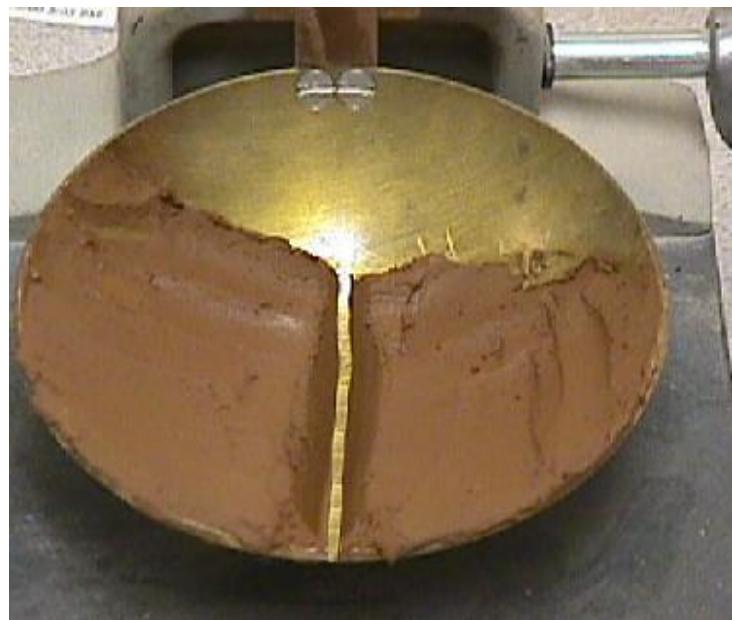
Figure 3-1: 13mm groove made in soil.

On the other hand, the lower limit of water content whereby a soil will exhibit plastic behavior is termed plastic limit (PL). At this stage, soils break into fragments upon remolding. The difference in water content between the liquid limit (LL) and plastic limit (PL) is the plasticity index, PI. i.e. PI= LL-PL.
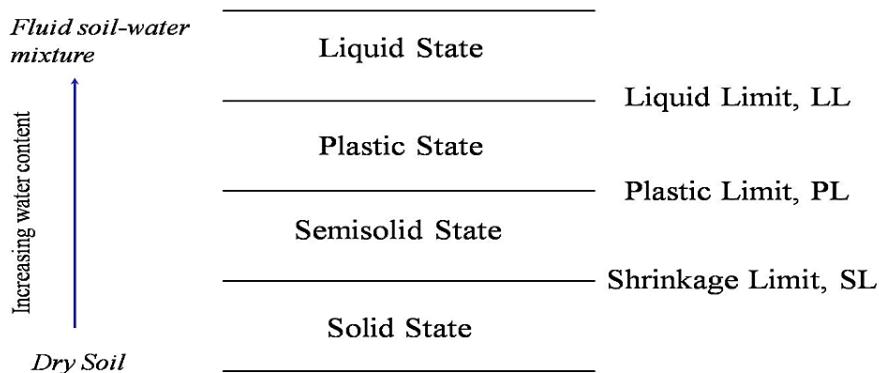
Figure 3-2: The four states of a soil with increasing water content.

3.2.2   Particle size distribution

Dry preparation, sieving and sedimentation were the techniques used in determining the particle size distribution of the seven representative soils. The sieving and sedimentation were done in accordance with ASTM D421 and ASTM 422 (2006) respectively. According to Das & Sawicki

39

(2001), particle size distribution involves the determination of the sizes range of particle size present in a soil, which is expressed as a percentage of the total dry mass.

The clay fraction within the soil samples was determined by hydrometer analysis. Fifty grams (50g) of the material passing through the number two hundred sieve (0.075mm) was dispersed for twenty-four hours in a one hundred and twenty-five milliliters (125ml) solution of sodium hexametaphosphate and deionized water. The resulting solution was then thoroughly mixed and poured into a jar up to the one thousand milliliters (1000ml) mark. The percentage passing is then calculated subtracting the cumulative percent retained from one hundred percent (100%). From the calculated results, a semi-logarithmic curve is plotted with the ordinary axis (arithmetic) being the percent fines and the aperture size as abscissa (logarithmic scale).

Further quantitative analysis of the slope and shape of the particle size distribution curve was done by means of the geometric values termed as the coefficient of uniformity (C_u) and the coefficient of curvature (C_c). The coefficient of uniformity (C_u) and the coefficient of curvature (C_c) can be expressed mathematically as:

$$C_u = \frac{D_{60}}{D_{10}} \text{ and } C_c = \frac{(D_{30})^2}{(D_{60} * D_{10})}$$

Where, D_{10} is the grain diameter (mm) corresponding to 10 percent passing on the particle size distribution curve. D_{30} is the grain diameter (mm) corresponding to 30 percent passing on the particle size distribution curve. D_{60} is the grain diameter (mm) corresponding to 60 percent passing on the particle size distribution curve (ASTM D421 2006). According to Craig (2004), soils with a larger range of particle sizes has a higher value of coefficient of uniformity. A soil is described as well graded if $1 \leq C_c < 3$.

3.2.3   Collapse potential test

A Collapse potential test was carried out on undisturbed soil samples in an oedometer (one-dimensional consolidation apparatus). Using the oedometer ring, a soil sample was carefully cut to avoid disturbance of the sample. Consolidation tests were carried out on these samples at their natural moisture content. Loads were applied incrementally from 25 kPa, 50 kPa, and 100 kPa up to 200 kPa via lever arm (Brink et al., 1982). When no further compression occurred at 200 kPa, the soil specimen was flooded with water and allowed to stand for twenty-four hours. Additional

stresses of 400 kPa and then 800 kPa were applied to the flooded samples. A logarithmic graph of void ratio against pressure (in kPa) was plotted. Jennings and Knight (1975) interpreted the results of all twelve samples using the guiding values of collapse potential.

The collapse potential of the soils was computed in accordance with ASTM D 5333 using the equation below:

$$CP = \left(\frac{\pm\Delta e}{1+e_0}\right) X\ 100\ \%$$

Where $\pm\Delta e$ is the difference in void ratio between unsaturated and saturated conditions with the positive and negative signs indicating swelling and collapse respectively and e_0 is the initial void ratio.

3.3   CT-SCAN TESTING METHODS

The CT-scan was used as part of this research to determine the porosity, void ratio, particle size distribution and pores size distribution of the reworked residual granites and residual Malmesbury shales. To obtain these parameters, 3D X-ray images were obtained using a General Electric Phoenix VTomeX L240 X-ray micro computed tomography scanner (microCT) and the NanoCT.

In order to achieve accuracy, multiple scans were performed on twelve (12) soil samples, six of these being undisturbed samples of reworked residual granites and residual Malmesbury shales in a 30mm X 150mm PVC pipes shown in Figure 3.3. The PVC containers ensured vertical stability. In addition, multiple scans were also performed on the remaining six (6) samples from the single oedometer test to investigate the microstructure after collapse. Furthermore, a total of eight (8) different reworked residual granites and residual Malmesbury shale soil samples were x-rayed and used to determine the particle size distribution.

The VGStudio Max version 2.2 coupled together with Avizo Fire image analysis software version 8.0 was used in filtering, classification and distribution of voids within the soil microstructure. The data obtained was used to calculate the porosity and void ratio. Lastly, CT scanning was used to confirm the particle size. This chapter also includes the various formulas, concepts and methods used in the various calculations and plots.
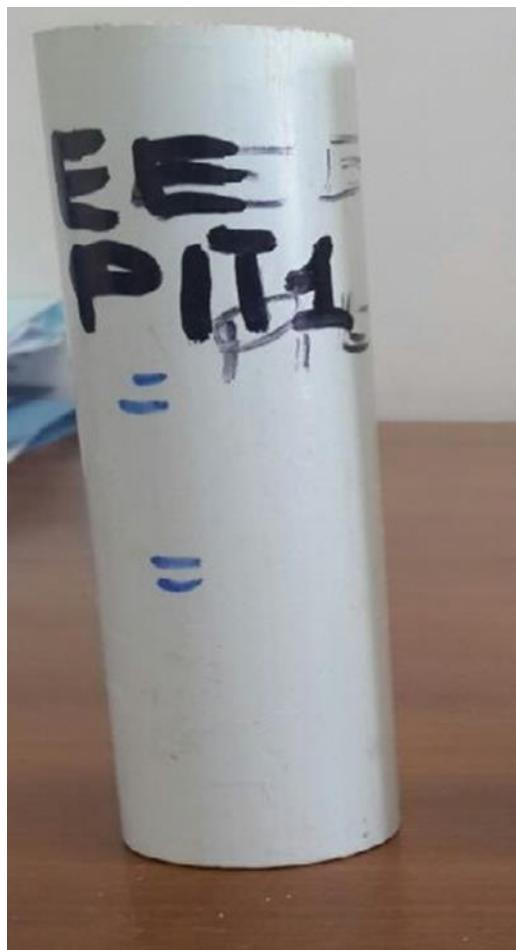
Figure 3-3: The 30mm X 150mm PVC containers ready for CT-Scan.

3.4   IMAGE PROCESSING METHODS

There are a number of image processing methods that can be applied to enhance the quality of images and data usefulness. An example of the image processing methods used for the determination of the porosity, void ratio and particle size distribution of the soil samples includes despeckling, thresholding, segmentation, erosion and dilation. This section provides a detailed explanation of the various image processing methods stated.

3.4.1   Determination of porosity and void ratio

The porosity of a soil sample is the ratio of the voids to its total volume. There are several methods to determine the porosity of soils, but CT-scanning has proven to have a higher detectability (Zion et al. 2014). However, the accuracy of the porosity values is highly dependent on the scanning and image analysis parameters (Kumar et al. 2012). Porosity determination of soil samples in CT

42

scanning processes involves four steps, which include despeckling, thresholding, demarcation of an area of interest and measuring the image (Nielsen, 2004).

Despeckling involves the removal of the extra pixel (noise) from a CT scan image after pores within the soil microstructure have been accurately detected. The despeckling filter measures the intensities of neighboring pixels within a 3x3 grid for each pixel in a numerical representation of a 2D image and then assigns the middle pixel the value of the median pixel intensity (Russ, 2002).

Thresholding is a form of segmentation. The process involves the separation of images into different sets of pixels, with the resulting image displayed as a two level image, using black and white or other colors. The choice of colors in thresholding is user dependent and/or the particular hardware in display.

In CT scanning, soil particles appear in different shades of gray that corresponds with each particle's density. With the aid of threshold filter, "solid spaces" gray is separated from "void spaces". The threshold filter takes a filter and an image with many pixel intensity values and returns the filtered pixels by replacing the pixels by either white or black. In an eight-bit monochrome digital image, this equals 255 grayscale values. Each pixel on the grayscale is assigned color intensity with the minimum zero (white) and the maximum equal to two hundred and fifty-six (black). A thresholded image consists of only white and black pixels which represents the solids and voids within the soil respectively.

The number of black and white pixels is directly dependent on the level of the threshold used. Low threshold values yield abundance of black pixels and vice versa. Therefore, by dividing the number of black pixels with the number of white pixels, the void ratio of an imaged soil from a CT scan can be obtained and vice versa for the porosity as shown in equations 1 and 2.

To reduce the edge effect and also to minimize the effect of changing volume, a region of interest (ROI) within the PVC canister is selected for analysis. In addition, by selecting the region of interest, the number of pixels can be counted by the aid of a histogram function. The porosity and void ratio from CT scan imaging can be determined from equations 3 and 4 below:

$$\text{Void ratio, e} = \frac{\text{(count at pixel value=0)}}{\text{(Count at pixel value=255)}} \qquad \text{Equation 1}$$

$$\text{Porosity, n} = \frac{\text{(count at pixel value=0)}}{\text{(count at pixel value=0) + (count at pixel value=255)}} \qquad \text{Equation 2}$$

3.4.2   Determination of particle size distribution

Granulometry is a process of computing the size distribution of objects from a digital image in terms of pixels using a series of morphological openings. Morphological opening is performed on a digital image with only black and white pixels to determine the particle size.

Erosion and dilation are the major processes in the morphological opening procedure. Erosion of a digital image is the intersection of image elements with the same structuring (size) element and dilation is the union of image elements with a given size element (Serra, 1982). The combination of the two steps (erosion and dilation) is the morphological opening procedure.

According to Serra (1982), dilation in general causes objects to grow in size by adding white pixels to the boundaries of the object in an image and then erosion suppresses the object by removing white pixels on the object boundaries. The number of white pixels added and or removed is dependent on the structuring element size and shape employed in the image processing. The structuring element is a reference shape of characteristic size, λ, for each opening used to probe the input image by removing pixel groups smaller than size λ. The size, λ, can have any arbitrary size and shape such as the diameter of a circle or the edge length of a square (Serra, 1982).

The number of pixels removed before and after morphological opening can be calculated by counting the foreground pixels for a complete opening procedure. The number of object features produced for a series opening iterations is smaller than a series of selected reference shape (for example the diameter of a circle). Serra (1982) described the size distribution of object features (size and shape) in a digital image as:

$$F_1 = 1 - \frac{G_{A(-\lambda)}}{G_A(0)}$$

Where F1 (λ) = the number of pixels removed for size λ.

G_A (-λ) = number of pixels removed (from size λ-1 to size λ).

$G_A(0)$ = the initial number of pixels in the image.

The pixel size is then converted to S.I units such as centimeters or millimeters from the scale of the CT scan image known. The processed data is sorted and exported to a spreadsheet to generate a grain size distribution plot.

3.5   SCANNING ELECTRON MICROSCOPE TESTING METHODS

The ZEISS EVO MA15 scanning electron microscope (photo of SEM included in Appendix D) at the Centre for Analytical Facility, Stellenbosch University was used for the morphological and mineral composition determination of the reworked granites and residual Malmesbury shales using a high vacuum mode. After sieving, three grams (3g) of each soil sample went through sample preparation comprising polishing and carbon plating.

Images were obtained by scanning the mounted sample with a focused beam. In short, after all the images were processed; they were then imported into a particle analysis program to examine the size, distribution and shape of the soil particles. The particle distribution obtained was compared to the traditional PSD and hydrometer analysis. The particle size data was presented in a histogram format. A total of one hundred and twenty samples was analyzed.

A multi-element analysis was performed on mounts using the ZEISS EVO MA15 microscope to ascertain the mineralogical composition. This was done to determine the effect of the mineralogical composition on the microstructure of the reworked residual granites as well as the residual Malmesbury shales.

3.5.1   Sample preparation

The sample preparation for the mineral identification for the microscopy study was categorized into three stages; namely polishing, carbon-plating and mounting. In order to obtain a representative image of the material particle distribution and mineral identification, careful sample preparation of the reworked residual granites and residual Malmesbury shales was done. Details of the sample preparation can be found in Appendix D. To hold the viewing plate firmly on the stage, a double sided tape is placed at the bottom part of each mount. A pressurized nitrogen gas is used to clean the chamber of the SEM. Images of the soil samples can then be obtained from the carbon-plated

mount. The mounts are carbon-plated so that the particle of the soil samples is charged for image acquisition as shown in Figure 3.4.

On the other hand, sample preparation for determination of the morphology of the particles was done by sticking the different particle sizes on a double sided tape placed on a glass slide, as shown in Figure 3.5. This method was chosen in order to have a clearer and wider view of the surface morphology.

Figure 3-4: Carbon-plated mounts of the soil samples for mineral identification.

Figure 3-5: Carbon-plated glass mounts for particle morphology analysis, (a) soil particle; (b) glass slide; (c) double sided tape.

3.5.2   Imaging and image analysis of sample

Background noise resulting from volume interaction in SEM images is one of the major challenges in microscopy. To reduce this effect, imaging of coarse and fine particles is done separately. Sample imaging was done with an acceleration voltage of twenty kilovolts (20 kV). The magnification and spot size were varied depending on the particle size. This was also done to obtain a clearer view of particles and allow easy measurement of each particle. Figure 3.6 depicts images taken at different magnifications. A total of one hundred and seventy images were taken for the mineral identification and the particle morphology analysis of individual particles.

Images were exported and saved on a hard drive for further processing using ImageJ image analysis software. To determine the outline of the aggregate particle, a threshold value was specified and the

actual image (initial gray image) was converted into a binary image (black or white pixels) with gray level intensities of zero (0) or two hundred and fifty-five (255) respectively. The object of interest (aggregate particles) with a gray scale value lower than the specified threshold value was set to black with a white background. Figure 3.7 shows an original image of aggregate particles and its corresponding binary image after thresholding. The output of the ImageJ analysis was used for the particle size distribution.
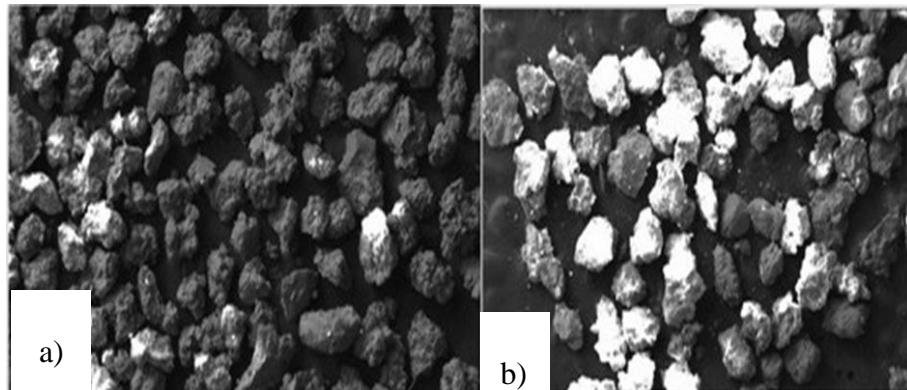
Figure 3-6: Secondary electron images of different particle sizes taken at different magnification a) 0.15mm particle size at a magnification of 38x b) 0.075mm particle size at a magnification of 22x.
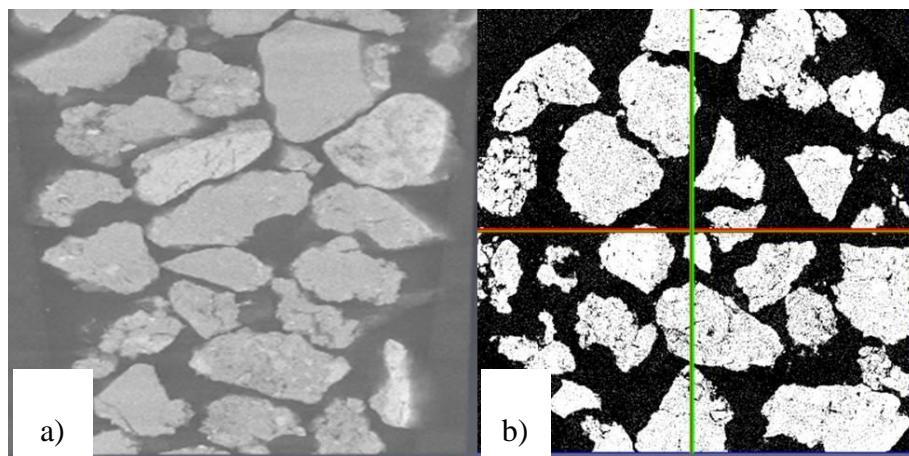
Figure 3-7: (a) An original image of aggregate particles and (b) its corresponding binary image after thresholding.

47

3.5.3   Determination of particle shape

The morphology of a grain that forms part of the earth fraction is termed particle shape. The sphericity and roundness were the two properties measured in this study. The sphericity of a particle is the ratio of the volume of the particle to the ratio of its circumscribing sphere and the roundness of a particle is a measure of the curvature of the corners and edges expressed as a ratio to the average curvature of the particle as a whole (Krumbein, 1941). The rapid measurement method suggested by Krumbein (1941) was used for the particle shape analysis and the interpretation was based on the "sphericity and roundness chart" (Santamarina et al. 2006) as shown in Figure 3.8. All the different particle sizes were taken at different magnifications with the resulting image saved. The images were printed and a minimum of two hundred particles, with twenty-five particles from each of the different grain sizes, were analyzed. Each particle was compared to the sphericity and a roundness model determination chart to determine its sphericity and roundness value. The number of particles compared was multiplied by its corresponding sphericity and roundness value. By dividing the sum of the sphericity and roundness value by the total number of particles analyzed, the arithmetic mean roundness was obtained as shown in the equation below:

$$\text{Roundness, P} = \frac{P*f}{\Sigma f}$$

Where f is the number of particles analyzed per size and Σf is the summation of the number of particles analyzed for all the different sizes.

$$\text{Sphericity, S} = \frac{S*f}{\Sigma f}$$

 Where f is the number of particles analyzed per size and Σf is the summation of the number of particles analyzed for all the different sizes.

$$\text{Roundness} = \frac{\Sigma_{ri}/N}{r_{max-in}}$$
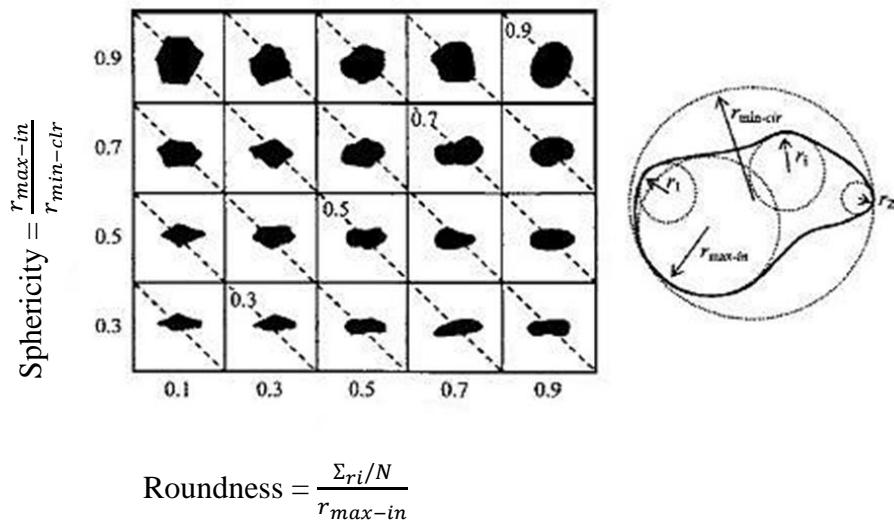
Figure 3-8: The sphericity and roundness chart (Cho et al. 2006)

3.5.4   Determination of mineral composition

The mineralogy of a soil plays a major role in soil characterization, and the formation of clay minerals, which either accelerates or decreases processes such as soil erodability, expansiveness, and collapsibility. To clearly differentiate between the different minerals, the backscattered electrons of the SEM were used to obtain the compositional information of the reworked residual granites and residual Malmesbury shales. An example of a backscattered electron image with the various mineral types is shown in Figure 3.9.

To obtain the backscattered electron image, a well-polished and carbon coated specimen as stated in section 3.5.1, was subjected to the beam from the x-ray source in the microscope chamber, monitored by the backscattered detector. The signal from the backscattered electron detector was used to regulate the gray level (brightness) of the image. The resulting imaged produced was the backscattered electron image.

49
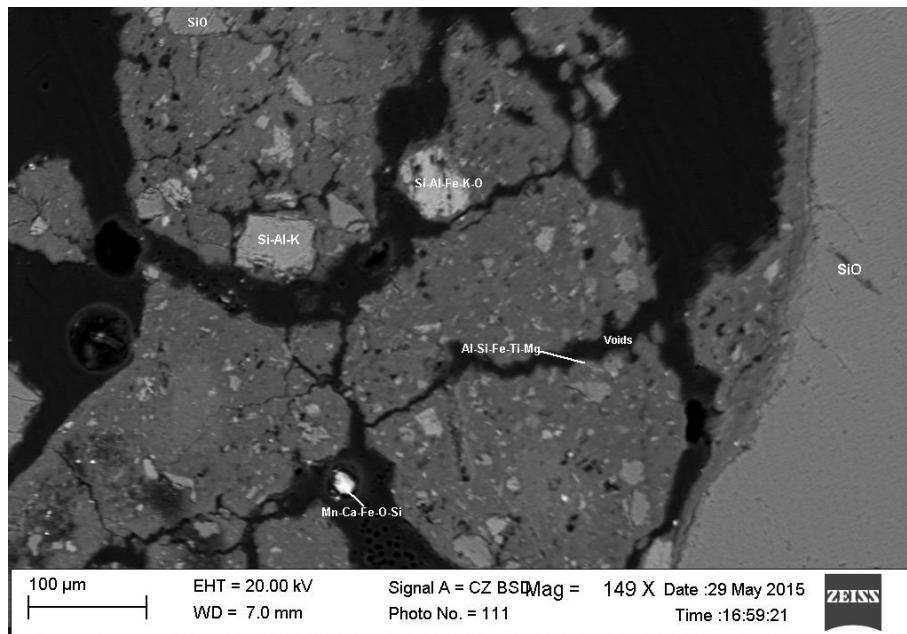
Figure 3-9: Backscattered electron image of a soil specimen with various minerals.

3.6   SAMPLING SITES

Two sites were demarcated for this study, namely Ernie Els Wines and Boland Bricks all within the Cape Winelands district municipality. Several factors motivated the researcher to choose the stated sites which includes: Conveniently situated in close proximity to the University of Stellenbosch, previous work conducted in the area showing evidence of collapsible soils and constraints with regards to permission to undertake the sampling process at a site in Kuilsriver.

A desk study was conducted for the two sites and relevant information was also gathered from the Council for Geoscience, the geology department of the University of Stellenbosch and personal discussions with experts in the field of geology.

3.6.1   Ernie Els Wines

Four undisturbed soil samples were taken from three different test pits (shown with red arrows) within Ernie Els Wines as shown in Figure 3.10. Samples were taken from between 0.7m and 1.2m depth below thin layers of alluvium. The sampling material comprised reworked residual granite.

Figure 3-10: An aerial photograph of Ernie Els Wines, Annandale Rd, Stellenbosch (courtesy Google imagery).

The farm is mainly underlain by coarse grain porphyritic granite with Malmesbury shales located in the western region of the farm. Granite outcrops were located 50m to the west of the test pitting area.

The samples from Ernie Els Wines were mostly moist, light brown to reddish brown, intact sandy silt with clay fractions. The SEM mineral composition shows that the coarse grained material was angular to sub angular quartz sand, weathered quartz and the clayey part composed of Kaolin.

3.6.2   Boland Bricks

Six undisturbed samples were taken from between 1.5m to 1.9m depth from three different test pits from the premises of Boland Bricks (shown with red arrows in Figure 3.11). The transported material comprising highly ferruginous laterite nodules overlying the residual Malmesbury shales.

Figure 3-11: An aerial photograph of Boland Bricks, Contractor Rd, Courtrai, Paarl (courtesy, Google imagery).

The main geology of the quarry was residual Malmesbury shales covered with laterites. The samples from Boland Bricks were moist and reddish to yellowish brown. The soil was intact, very dense and laminated.

3.7   SAMPLING METHODS

Soil samples were obtained from two sampling locations. The locations were chosen based on previous work done in the area, a desk study using topographic and geological maps and personal communication with Dr. Jurie Viljoen (Council for Geoscience), and Mr. Leon Croukamp and Mrs. Nanine Fouché from the University of Stellenbosch.

A total of six test pits were excavated using a tractor-loader-backhoe (TLB). Three of these were excavated at Ernie Els Wines and three at Boland Bricks in Paarl, within the Stellenbosch Municipality.

In order, to obtain undisturbed samples of the reworked residual granites, 250mm (diameter) x 300mm (length) PVC pipes with a wooden base were used. To avoid major disturbance, the sampling container was slowly pushed and rotated into the soil. A total of four undisturbed samples were taken for laboratory testing; one from each test pit. Due to the dense nature of the residual Malmesbury shale, block samples were carved out from the in-situ material, as described by

Jennings and Knight (1975).   A total of six undisturbed blocked samples were obtained. To avoid moisture loss, all samples were wrapped and covered with sealed plastic bags before being transported to the laboratory.

3.8   SOIL PROFILING

According to Schwartz, visual inspection, a non-destructive technique in soil profiling, is the first step in identifying a potential collapsible soil in the field. Identification was done using a soil sampling sheet and an observation checklist. This includes the moisture condition, consistency, color, structure, soil type, and origin. Appendix A provides details of the soil profiles of all seven test pits. The descriptions were done as proposed by Jennings et al. (1973).

CHAPTER 4. RESULTS AND DISCUSSION

4.1   INTRODUCTION

As previously stated in Chapter 3, the experimental work was broadly categorized into two phases, of which the first phase was the traditional geotechnical laboratory test which included sieving, hydrometer analysis, collapse potential testing and the determination of the Atterberg limits. The second phase termed "alternate methods" as described by the researcher included x-ray computed tomography and scanning electron microscopy. Discussion and analysis of the results obtained from both phases are presented in this chapter.

4.2   ATTERBERG LIMITS AND PARTICLE SIZE DISTRIBUTION

Determination of the Atterberg limit and particle size distribution (mechanical sieving and hydrometer analysis) were undertaken to help in the description and classification of the soil samples used in the experimental work. The description and classification was based on the Unified Soil Classification system (USCS). A summary of the engineering properties of each of the six test pits is presented in Table 4.1 and Table 4.2.

Furthermore, the results from the collapse potential tests were used, together with the engineering properties from Table 4.1 and Table 4.2, to determine which of the two soil types (reworked residual granite and residual Malmesbury shale) is potentially collapsible.

Table 4-1: Engineering properties of reworked residual granites, Ernie Els Wines.

Sample Properties	Pit 1	Pit 2	Pit 3
Depth (m)	0.50	0.7	1
Clay (%)	0*	0*	0*
Silt (%)	3	2	2
Sand (%)	71	68.5	71
Gravel (%)	26	29.5	27
Liquid Limit (LL)	43.53	35.87	43.66
Plastic Limit (PL)	28.04	31.57	27.77
Plasticity Index (PI)	15.49	4.31	15.89
Difference in sand and clay proportion (%)	71	68.5	71
Unified Soil Classification System	ML	ML	ML

* A very low clay content in soil rounded to 0%.

Table 4-2: Engineering properties of residual Malmesbury shales, Boland Bricks

Sample Properties	Pit 1	Pit 2	Pit 3
Depth (m)	1.0	1.5	1.3
Clay (%)	54	48	52
Silt (%)	46	52	48
Sand (%)	0	0	0
Gravel (%)	0	0	0
Liquid Limit (LL)	31.97	35.91	47.65
Plastic Limit (PL)	25.26	31.05	39.73
Plasticity Index (PI)	6.71	4.86	7.91
Unified Soil Classification System	ML-OL	ML-OL	ML-OL
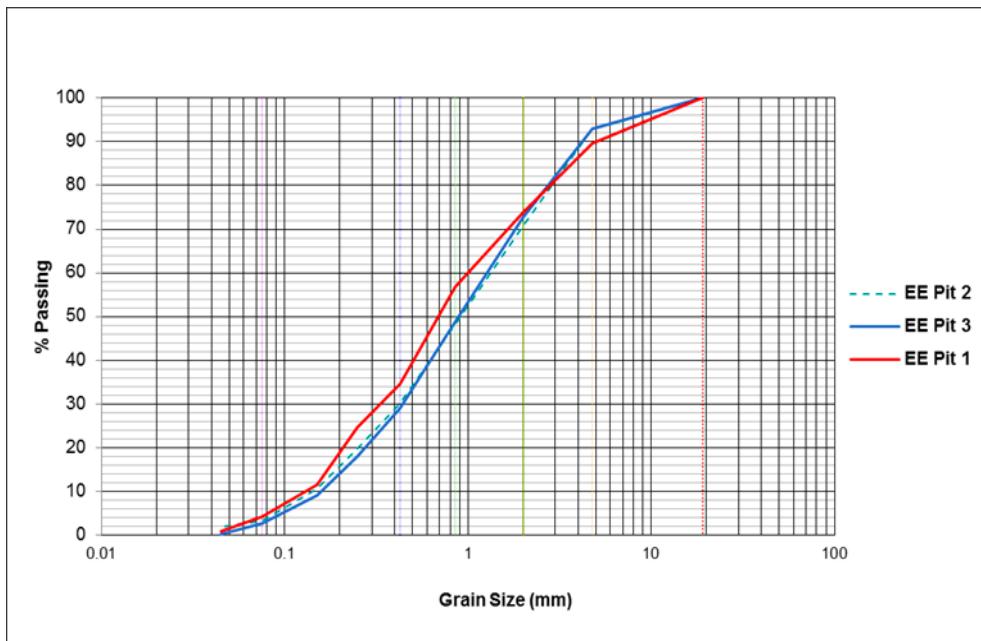
Figure 4-1: Ernie Els Wines grain size distribution.

The above graph (Figure 4.1) indicates that, the soil from Ernie Els Wines (EE) pit 1 constituted 71% sand and 3% silt with a significant proportion of gravel, 26% (see Table 4.1). The soil from Ernie Els Wines pit 1 can be classified as poorly graded sandy gravel (GP) with low plasticity.

From the graph above (Figure 4.1), 98% of the soil from EE pit constituted sand and gravel with a very low fines content. The soil sample can be classified as poorly graded sandy gravel (GP) with low plasticity.

It can be deduced from Figure 4.1 that the soil sampled from EE pit 3 comprise 71% sand and 27% gravel with only 2% fines. The soil from pit 3 is poorly graded can therefore be described as sandy gravel with low plasticity (GP) based on their grading and plasticity.
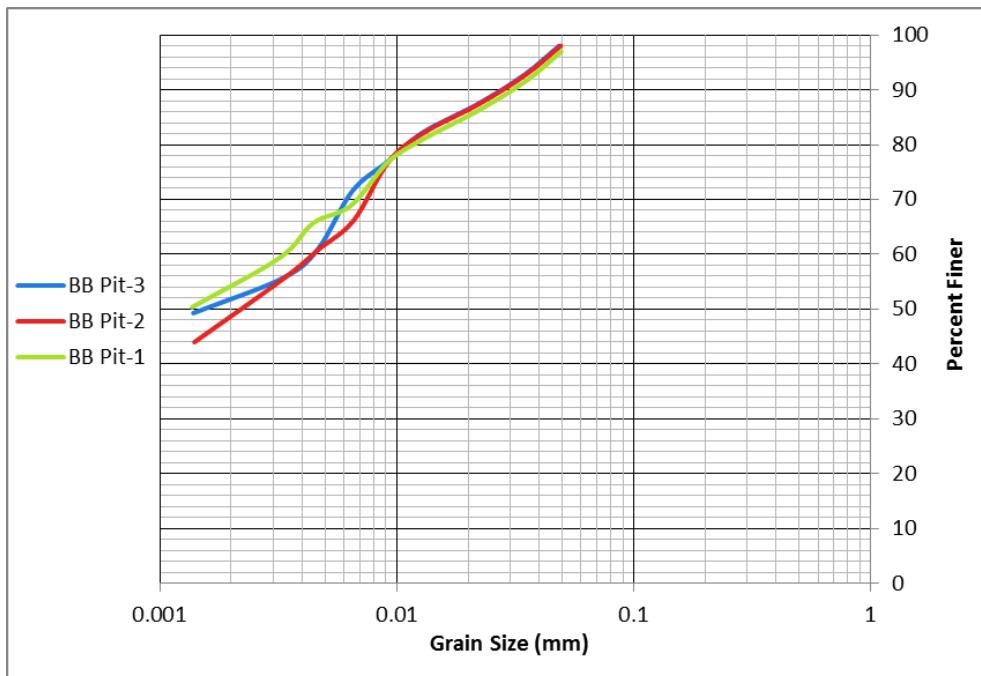
Figure 4-2: Grain size distribution of residual Malmesbury shales.

The graph in Figure 4.2 shows that more than half of the soil content from pit 1 is clay (54%) with a significant quantity of coarse to fine silt (46%). The soil from Boland Bricks pit 1 can be classified as a silty clay with low plasticity (ML).

On the other hand, the soil from pit 2 constituted 52% silt and 48% clay. From Table 4.1, the soil from Boland Bricks pit 2 can be classified as a silty clay with low plasticity (ML-OL).

The soil from Boland Bricks pit 3 can be classified as a silty clay with low plasticity (ML-OL). This is because a greater percentage of the soil constituted clay (52%) with a significant proportion of silt (48%).

From Figure 4.2, Table 4.1, and Table 4.2, it is evident that the residual Malmesbury shales from Boland bricks have higher clay contents than the reworked residual granite from Stellenbosch

4.3   COLLAPSE POTENTIAL RESULTS

Collapse potential tests were conducted on both the reworked residual granites from Ernie Els Wines and the residual Malmesbury shales from Boland Bricks. The collapse potential test was used as an index test (Schwartz, 1985) to guide the researcher to determine which of the two soil

57

types is susceptible to collapse. Moreover, the results from the collapse potential test coupled with the three dimensional (3D) images from CT-scanning gave the researcher a clearer picture of the microstructure properties of the two soil types in question.
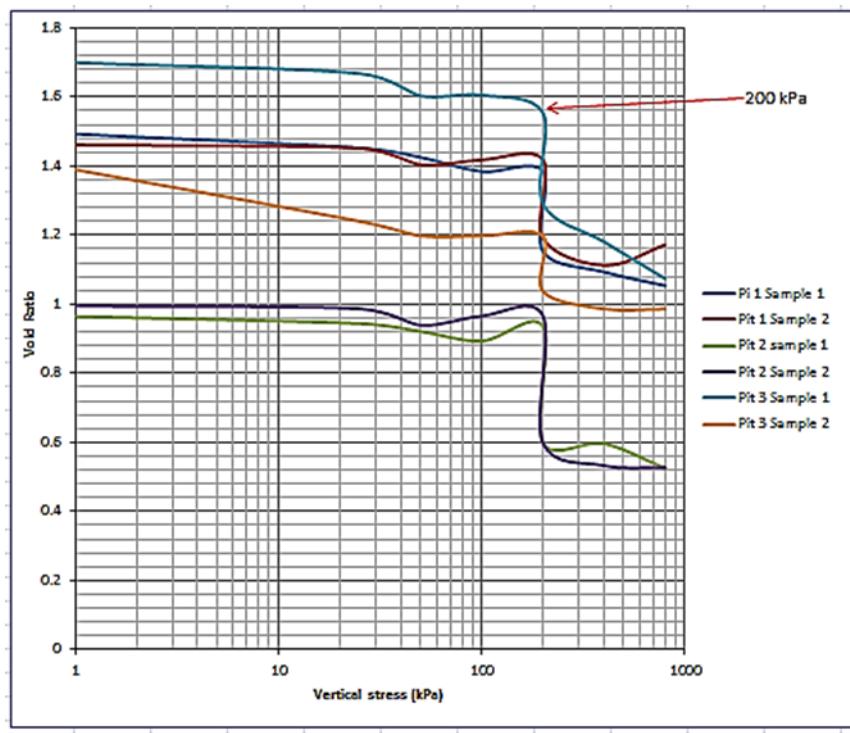
Figure 4-3: Void ratio versus vertical stress of Ernie Els Wines test pits

From the graph above (Figure 4.3), it can be deduced that all six samples started to yield at 25 kPa. Moreover, almost all the samples showed signs of swell before collapse upon saturation at 200 kPa. All six samples collapsed upon saturation at 200 kPa. This result was anticipated because of the reasons below.

The problems with collapse are generally associated with silty or sandy soils with low clay content (Brink et al., 1982). This was evident in the Atterberg limits and particle size distribution curves of all the soil sampled from Ernie Els Wines farm (see Table 4.1). The different grain sizes of the reworked residual granites were bridged together by the very fine silt. This created a honeycomb structure (porous structure within the soil matrix). A three dimensional (3D) image of the honeycomb structure is shown in Figure 4.14 (a). Upon saturation and loading, the very fine silt are washed out to fill the voids within the porous structure. This led to particle rearrangement leading to collapse.

58

Another contributing factor is the presence of feldspar, smectite clay, kaolin clay and quartz making up the matrix within the reworked residual granite (see Table 4.19). Kaolin clay, feldspar, and quartz sand formed by weathering, are easily leached and eroded (Dippenaar et al. 2006). The reworked residual granites exhibit a collapsible grain structure after extensive leaching and erosion of this finer matrix material.

Basma and Tuncer (1992) concluded from their study that, with regard to soil type, a higher coefficient of uniformity (Cu) indicates a higher collapse potential (CP %). Likewise, at specific stress levels, the difference between percentage of sand and clay in the soil is directly proportional to the collapse potential. Soil samples from pit 2 had the highest Cu (9.4) compared to that of pit 1 (7.1) and pit 3 (7.8), and hence the highest collapse potential (17.76), according to Basma and Tuncer (1992).

From Table 4.1, pit 1 and pit 3 from Ernie Els Wines had the largest difference in sand and clay ratio and CP % ratio as seen in the graph shown in Figure 4.4. Pit 2 had the highest collapse potential (18.40%) due to the greater percentage of gravel. The greater percentage of gravel created a more porous structure.
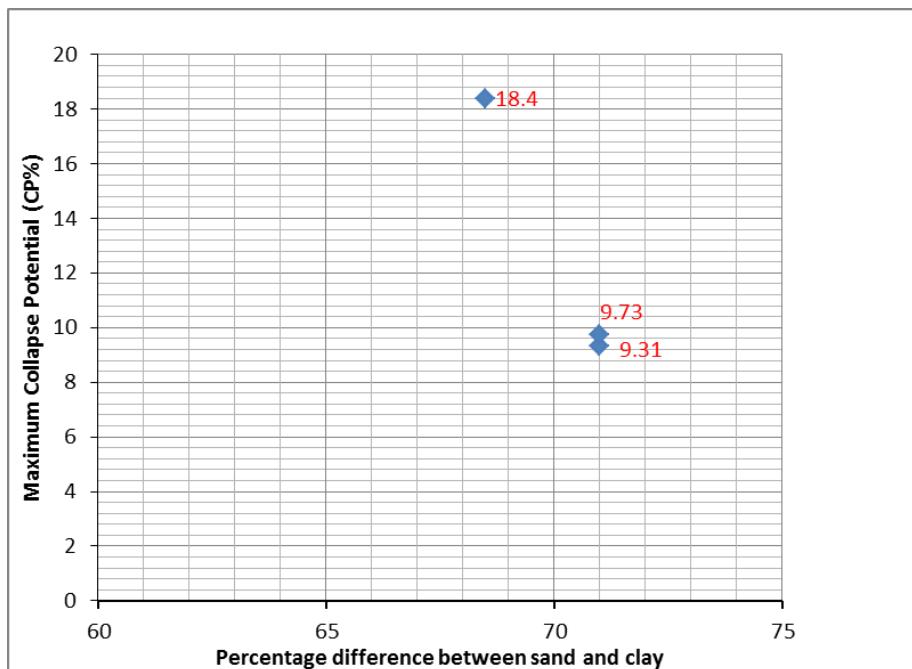
Figure 4-4: Maximum collapse potential versus percentage difference between sand and clay for reworked residual granite.

59

According to Jennings and Knight's (1975) classification, the severity of the collapse of the reworked residual granite from pit 2 and its effects on a foundation can be described as "severe problem" with an average collapse potential (CP %) value of 17.76. Reworked residual granites from pit 1 and Pit 3 had average CP % values of 9.29 and 8.23 respectively. Reworked residual granite from pit 1 and pit 3 are classified as a "problem" according to Jennings and Knight's (1975).
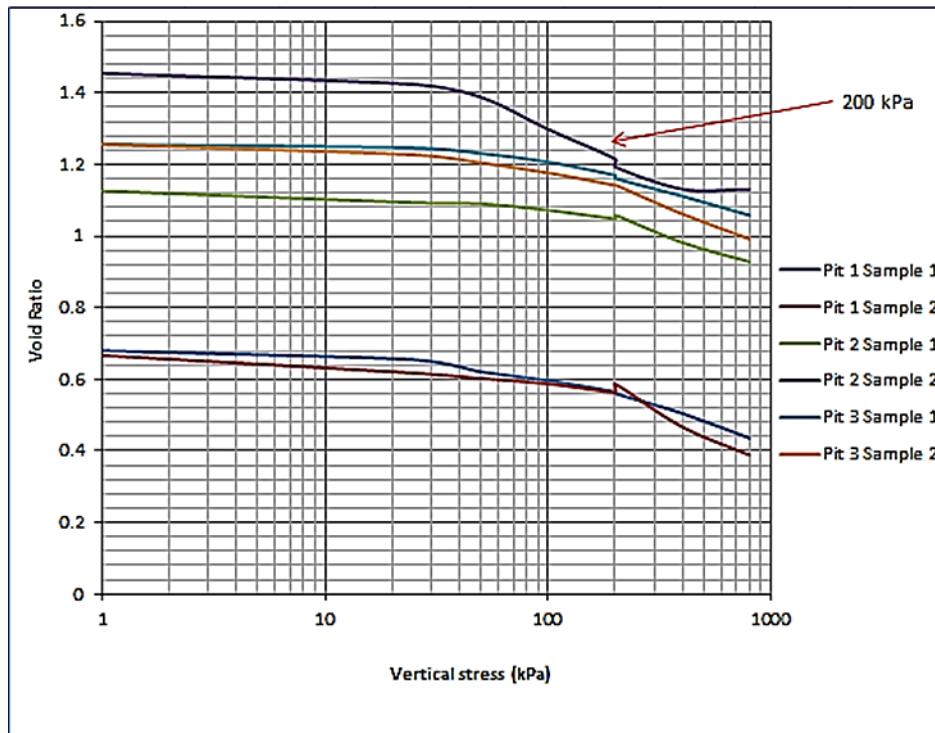
Figure 4-5: Void ratio versus vertical stress of Boland Bricks test pits.

Figure 4.5 represents the collapse potential test of soil specimen from Boland Bricks test pits. The poorly sorted fine grained sediments (clay and silt sized) filling the voids, creates a smaller pore throat (small pore space at the point where two grains/particles meet, which connects two larger pore volumes). This decreases the porosity and permeability within the soil matrix and hence its ability to sustain high stresses without any form of settlement, as shown in Figure 4.5.

Another contributing factor is the preferred orientation of the clay particles which in the case of the residual Malmesbury shale is laminated to the deposition. This reduces the voids within the soil matrix and hence hinders the formation of a collapsible fabric which is a critical condition leading to collapse.

Porosity increases with the roundness of grains, but the scan images from Figure 4.6 shows that the clay sized particles are platy and hence forming a well layered and packed grains reducing voids within the soil matrix.

From Figure 4.5, it can be deduced pit 1 sample 2, pit 2 sample 1 and pit 3 sample 2 showed signs of heave at 200 kPa. Heaving is the upward swelling of soils. This can be attributed to the change in volume of the clay content during the inundation of water at 200 kPa.
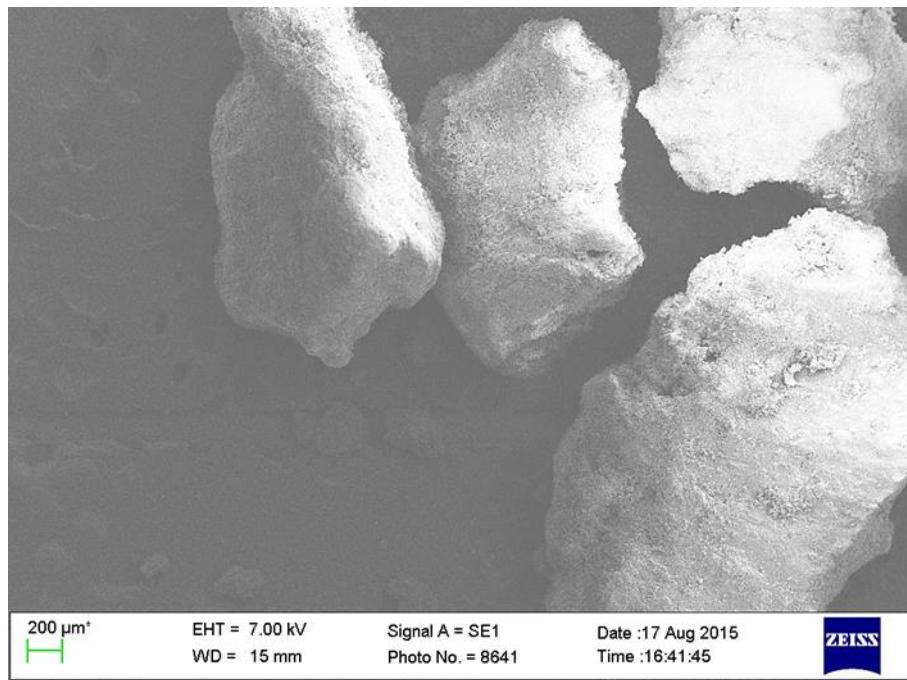
Figure 4-6: SEM images of residual Malmesbury shale, Boland Bricks.

Although the soil specimen from test pit 2 of the residual Malmesbury shales had the highest percentage of fines as recorded in Table 4.1 it also displayed the highest collapse potential (0.89) of the residual Malmesbury soils (see Table 4.4).

According to Jennings and Knight's (1975), all the residual Malmesbury shales from Boland Bricks can be classified as non-problematic. This result was anticipated due to the platy grain texture, poorly sorted particles (high fine content), and grain mineralogy.

Table 4-3: Packing properties of residual granite from Ernie Els Wines.

Sample Properties	Pit 1 Sample 1	Pit 1 Sample 2	Pit 2 Sample 1	Pit 2 Sample 2	Pit 3 Sample 1	Pit 3 Sample 2
Max void ratio (before test)	1.49	1.46	0.96	0.99	1.69	1.40
Min void ratio (after test)	1.05	1.11	0.53	0.53	1.07	1.00
Average void ratio	1.31	1.33	0.80	0.81	1.46	1.20
Collapse potential (CP %)	9.31	9.26	17.11	18.40	9.73	6.73
Maximum collapse potential (CP%)	9.31		18.40		9.73	
Average collapse potential (CP %)	9.29		17.76		8.23	

Table 4-4: Packing properties of residual Malmesbury shales from Boland Bricks.

Sample Properties	Pit 1 Sample 1	Pit 1 Sample 2	Pit 2 Sample 1	Pit 2 Sample 2	Pit 3 Sample 1	Pit 3 Sample 2
Max void ratio (before test)	0.68	0.67	1.13	1.45	1.26	1.26
Min void ratio (after test)	0.44	0.39	0.93	1.13	1.06	1.00
Average void ratio	0.58	0.56	1.05	1.28	1.20	1.15
Collapse potential (CP %)	0.26	-1.35*	-0.47*	0.89	0.36	-0.06*
Maximum collapse potential (CP %)	0.26		0.89		0.36	
Average collapse potential (CP %)	-1.10*		0.42		0.30	

*Sample displayed heave.

63

4.4   CT-SCANNING RESULTS

4.4.1   Introduction

One of the objectives of this research was to develop a testing method to determine the soil index properties of potentially collapsible soils using images produced by CT-scanning. The General Electric Phoenix VTomeX L240 X-ray micro computed tomography scanner (microCT) and the NanoCT of the center for analytical facility at the University of Stellenbosch was used to produce both two-dimensional (2D) and three-dimensional 3D images which were used to determine the particle size distribution, porosity and pore size distribution.

4.4.2   CT-Scanning Images

To determine the soil index properties using CT scanning, the first step was to obtain quality images of the soil samples. Images produced for this research was in two-dimensional (2D) and three-dimensional (3D) view. The image quality was determined by the spacing between the x-ray source and the sample and the container size. Figure 4.7 shows an example of CT-scanned images of soil samples.
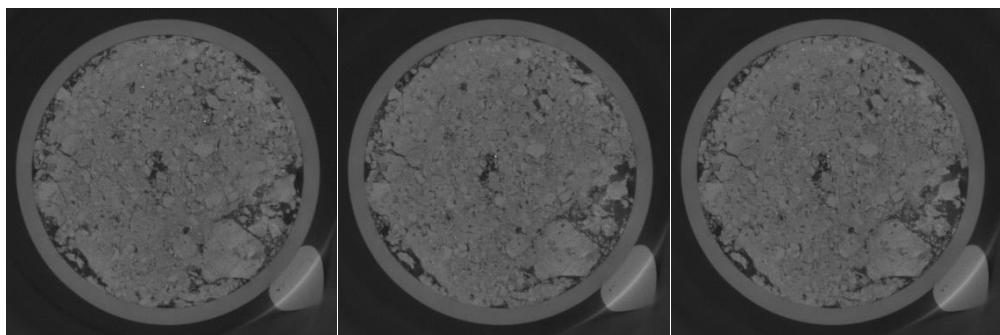
Figure 4-7: Ernie Els Wines reworked residual granites CT scans.

4.4.3   Soil porosity

Soil porosity is the ratio of the voids to its total volume. In this research, the porosities of the six (6) undisturbed soil samples were measured using CT-scanning test procedures described in Chapter 3. Images produced from the scanning process were processed and used to calculate the porosity in

terms of the volumetric change of the reworked residual granites and residual Malmesbury shales before and after consolidation. The size of the different types of pores within each sample was determined based on Brewer's (1964) pore size classification, which is shown in Table 4.5. The pore size classification was used together with the average volumetric change during the collapse of both reworked residual granite and residual Malmesbury shales to display the degree of collapse. This pore sizes and volume changes are shown in Table 4.6 through to Table 4.8.

Table 4-5: Morphological and pore size classification (Brewer, 1964).

Diameter [µm]	Class Limit	Subclass
> 5000		Coarse
2000 - 5000		Medium
1000 - 2000	Macropores	Fine
75 - 1000		Very fine
30 - 75	Mesopores	
5 - 30	Micropores	
0.1 - 5	Ultramicropores	
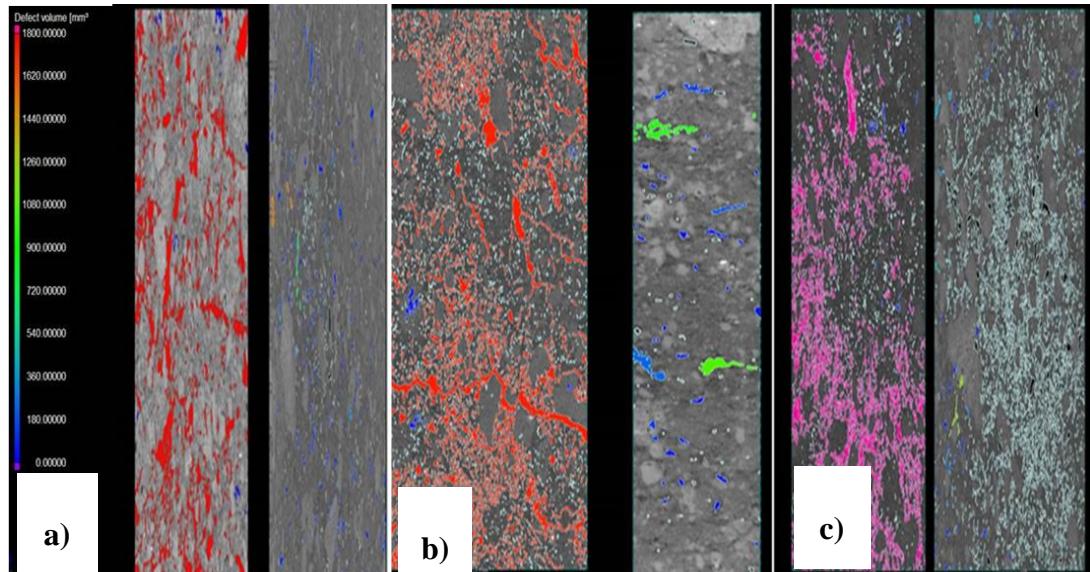
Figure 4-8: Thresholding applied to sliced two-dimensional (2D) image volumetric change a) pit 1, b) pit 2 and c) pit 3.

65

Table 4-6: Morphological pore size classification, Ernie Els Wines Pit 1 (modified after Brewer, 1964).

Diameter [μm]	Class Limit	Subclass	Average Volume (undisturbed sample) [mm³]	Average Volume (after the collapse) [mm³]
> 5000	Macropores	Coarse	313.26	2.31
2000 - 5000		Medium	0.34	0.39
1000 - 2000		Fine	0.15	0.15
75 - 1000		Very fine	0.11	0.13
30 - 75	Mesopores		N/A	N/A
5 - 30	Micropores		N/A	N/A
0.1 - 5	Ultramicropores		N/A	N/A

From Table 4.6, there was a reduction in the average volume of the coarse macropores from 313.26 mm^3 to 2.31 mm^3 showing a clear indication of collapse settlement in Ernie Els Wines pit 1. There was an increase in the average volume of the medium and very fine macropores after the collapse though not very significant. This was due to the particle rearrangement after collapse. This led to the formation of smaller voids as shown in Figure 4.8 (a).

Table 4-7: Morphological pore size classification, Ernie Els Wines Pit 2 (modified after Brewer, 1964).

Diameter [µm]	Class Limit	Subclass	Average Volume (undisturbed sample) [mm³]	Average Volume (after the collapse) [mm³]
> 5000	Macropores	Coarse	2,408.32	2.44
2000 - 5000		Medium	0.25	0.44
1000 - 2000		Fine	0.15	0.17
75 - 1000		Very fine	0.12	0.11
30 - 75	Mesopores		N/A	N/A
5 - 30	Micropores		N/A	N/A
0.1 - 5	Ultramicropores		N/A	N/A

The maximum collapse potential for pit 2 can be attributed to the large average volume of the coarse macropores of the undisturbed soil sample in Table 4.7. The average volume of the coarse macropores reduced from 2,408.32 mm^3 to 2.44 mm^3 upon saturation and additional loading. There was a significant increase in the average volume of the medium macropores and the fine macropores as a result of the formation new voids of smaller volumes as depicted in Figure 4.8 (b). The formation of the new voids of smaller average volumes can also be attributed the blocking of the pore throat by fine particles as a result of the particle rearrangement during collapse settlement.

Table 4-8: Morphological pore size classification, Ernie Els Wines Pit 3 (modified after Brewer, 1964).

Diameter [μm]	Class Limit	Subclass	Average Volume (undisturbed sample) [mm³]	Average Volume (after the collapse) [mm³]
> 5000	Macropores	Coarse	379.36	2.11
2000 - 5000		Medium	0.27	0.41
1000 - 2000		Fine	0.15	0.15
75 - 1000		Very fine	0.00	0.14
30 - 75	Mesopores		N/A	N/A
5 - 30	Micropores		N/A	N/A
0.1 - 5	Ultramicropores		N/A	N/A

From Table 4.8, it is clear that the average volume of the coarse macropores in the soil sampled from test pit 3 at Ernie Els Wines reduced from 379.36 mm^3 to 2.11 mm^3 upon saturation and additional loading. There was a one hundred percent increase in the average volume of the medium macropores and the very fine macropores. The x-ray images in Figure 4.8 (c) show the change in voids after collapse of reworked residual granites from Ernie Els Wines pit 3. The change in the average volume of macropores is due to particle rearrangement and the formation of new voids after collapse.

It can be concluded that volumetric changes only occur within the macropores of the reworked residual granites. In addition, the calculated average volume of the coarse macropores decreased after collapse. The Sliced 2D images and 3D images show that, for collapse settlement to occur, the voids must be well connected.

Table 4-9: Morphological pore size classification, Boland Bricks Pit 1 (modified after Brewer, 1964).

Diameter [μm]	Class Limit	Subclass	Average Volume (undisturbed sample) [mm³]	Average Volume (after the collapse) [mm³]
> 5000	Macropores	Coarse	9.96	2.50
2000 - 5000		Medium	0.18	0.24
1000 - 2000		Fine	0.12	0.13
75 - 1000		Very fine	0.00	0.12
30 - 75	Mesopores		N/A	N/A
5 - 30	Micropores		N/A	N/A
0.1 - 5	Ultramicropores		N/A	N/A

From Table 4.9, it is evident that there are minimal average volumetric change of pores within the soil specimens of Boland Bricks pit 1. This explains the low CP obtained for the residual Malmesbury shales.

Table 4-10: Morphological pore size classification, Boland Bricks Pit 2 (modified after Brewer, 1964).

Diameter [μm]	Class Limit	Subclass	Average Volume (undisturbed sample) [mm³]	Average Volume (after the collapse) [mm³]
> 5000	Macropores	Coarse	386.16	48.17
2000 - 5000		Medium	0.35	0.24
1000 - 2000		Fine	0.15	0.14
75 - 1000		Very fine	0.12	0.12
30 - 75	Mesopores		N/A	N/A
5 - 30	Micropores		N/A	N/A
0.1 - 5	Ultramicropores		N/A	N/A

Although Boland Bricks pit 2 was classified as non-collapsible, it is evident from Table 4.10 that the soil specimen undergoes a volumetric change from 386.16 mm^3 to 48.17 mm^3 (less volume change than reworked residual granite from Ernie Els Wines pit 3 where it changed from 379.36 mm^3 to 2.11 mm^3) within the coarse macropores and the medium macropores. The average volumetric change of the coarse to fine macropores decreased due to applied loads during the collapse potential test.

Table 4-11: Morphological pore size classification, Boland Bricks Pit 3 (modified after Brewer, 1964).

Diameter [µm]	Class Limit	Subclass	Average Volume (undisturbed sample) [mm³]	Average Volume (after the collapse) [mm³]
> 5000	Macropores	Coarse	31.98	33.35
2000 - 5000		Medium	0.74	0.41
1000 - 2000		Fine	0.19	0.16
75 - 1000		Very fine	0.11	0.12
30 - 75	Mesopores		N/A	N/A
5 - 30	Micropores		N/A	N/A
0.1 - 5	Ultramicropores		N/A	N/A

From Table 4.11, it can be seen that a soil specimen from Boland Bricks pit 3 undergoes a volumetric change in the medium to fine macropores. The average volume of the medium to fine macropores decreased from 0.74 mm^3 to 0.41 mm^3 and 0.11 mm^3 to 0.12 mm^3 respectively. On the other hand, the average volume of the coarse macropores increased to 33.35mm^3 after the collapse potential test. This result was unexpected and can be attributed to cracks which developed within the soil sample during the collapse potential test. This is shown in the CT-scan image in Figure 4.9.

None of the three (3) pits from Boland Bricks was classified as collapsible. The following conclusions were reached after studying the porosity in relation to the volumetric changes within the microstructure of the soil samples from Boland Bricks:

- Cracks within the soil samples also contributed to an increase in the average volume of pores calculated from the CT-scanning data.
- Volumetric changes occur within the macropores.
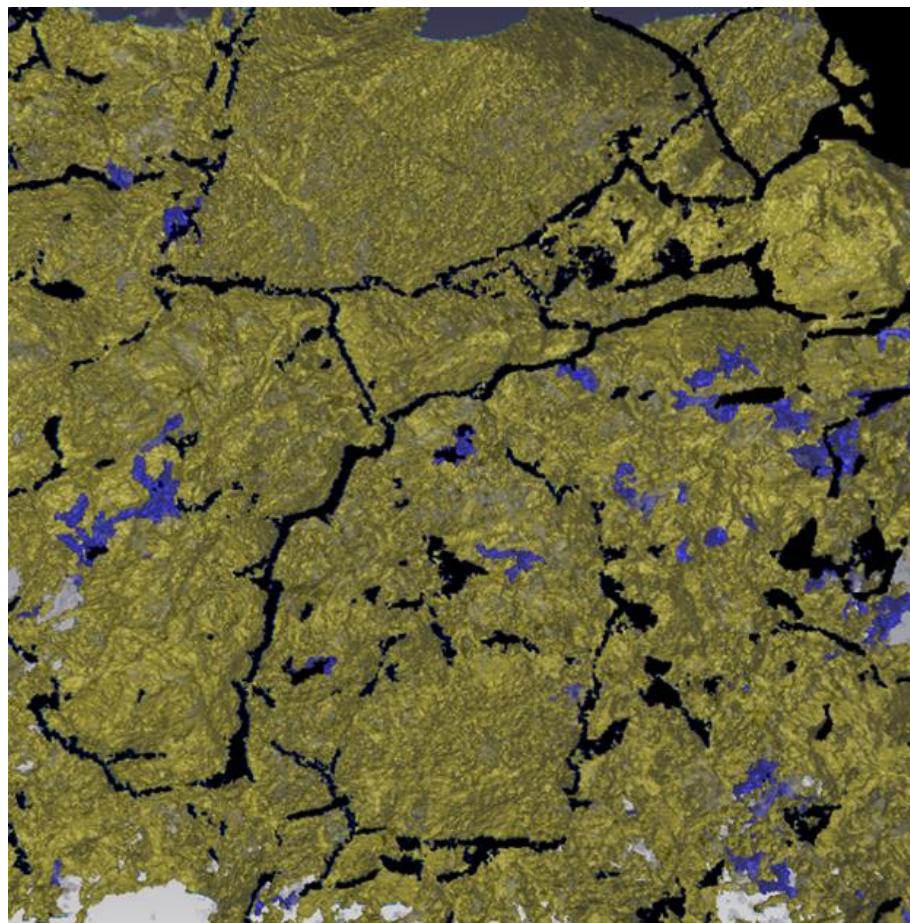
Figure 4-9: CT-scan image showing cracks within the soil specimen.

4.4.4   Particle size distribution

Ten (10) CT-scanned soil samples were analyzed for particle size distribution (PSD). To obtain a wider distribution of different particle sizes within the canister, a region of interest (ROI) was selected. This was achieved by crop editing a section with a 750mm (width) X 750mm (length) X 1500mm (height) dimension within the canister. The PSD analysis was done using an image processing technique termed granulometry using Avizo Fire version 8.0. Detailed explanation of the granulometry process was done in Chapter 3, section 3.4.2. The calculated grain sizes from the CT-

scanning process was averaged and compared to the measured PSD by mechanical sieving. The plot of the CT-scan PSD and the mechanical sieving PSD is shown in Figure 4.10.
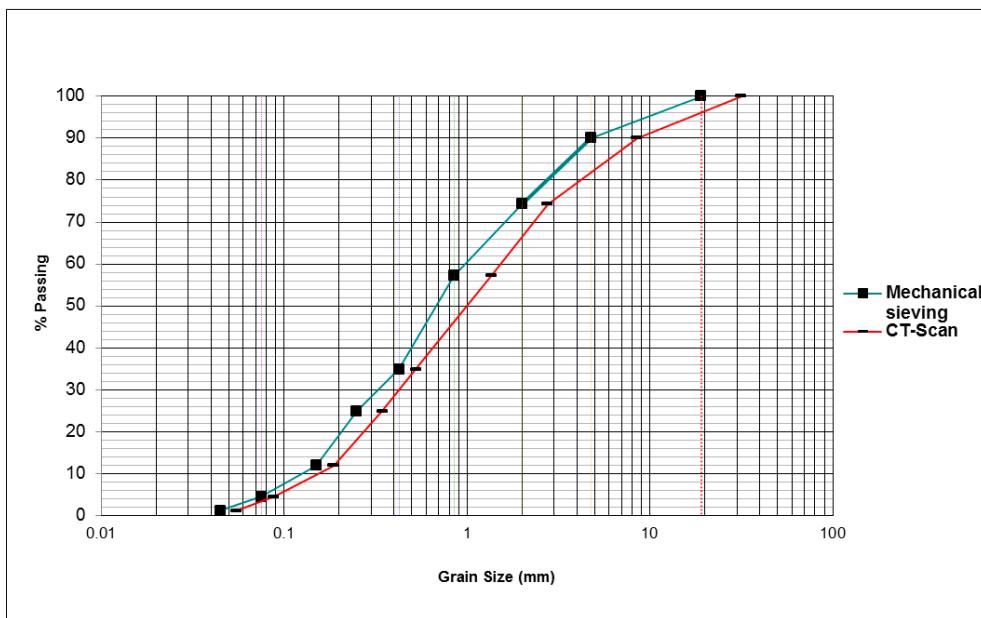
Figure 4-10: Particle size distribution of reworked residual granite from Ernie Els Wines pit 1.

It can be observed from Figure 4.10 that there are some discrepancies between CT-Scan and mechanical sieving particle size distribution. This can be attributed to the following:

The measured CT-scan particle size in Figure 4.10 seems larger than the measured mechanical sieve particle size. This occurs when very fine particles (silt) clump together and are then sent in a digital image as a single homogenous particle. This makes individual particles blurry. This error in the image is termed bleeding. Figure 4.11 (a) shows an original digital image and Figure 4.11 (b) a thresholded image with a bleeding effect.

In addition, the parameters retrieved from CT-scan images using Avizo Fire version 8.0 includes the volume and area of the individual particles within the ROI. The actual diameter of each particle/grain can be calculated from either the volume or area as obtained from Avizo Fire version 8.0. Therefore, CT-scan measured coarse particles are more accurate than particles measured in mechanical sieving, which operates on a mass-based result instead of particle diameter. On the other

72

end, the measured particle size for finer particles is more accurate in mechanical sieving than in CT-scanning.

Another possibility for the discrepancy is the particle shape. Particle size distribution of finer material (<150µm) when using dry sieving will yield significantly less accurate results. This can be attributed to the fact that, in sieve analysis, particles are assumed spherical and this is not true for all particles. In addition, needle or rod like particles will either pass through the sieve or remain behind on the sieve, depending on its orientation.
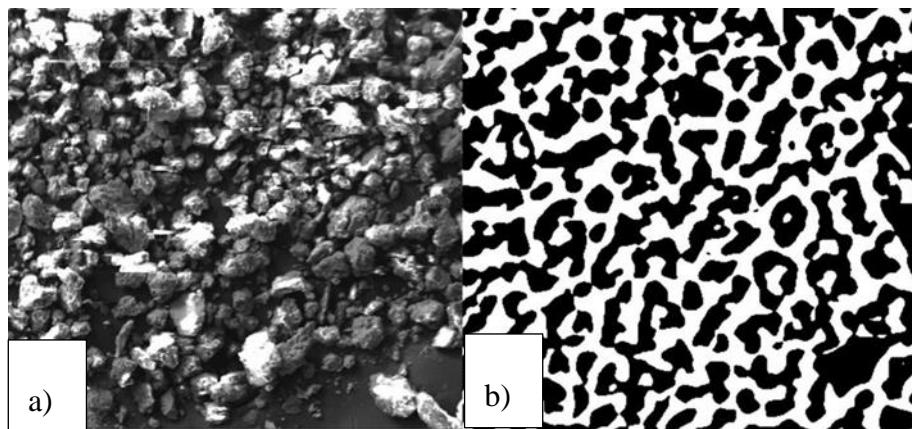
Figure 4-11: (a) original digital image and (b) a thresholded image with bleeding effect.

Although there are some discrepancies in the graph in Figure 4.10, yet both CT-scan and mechanical sieving produced similar grading and mechanical properties for the reworked residual granites as shown in Table 4.12. The measured PSD from both CT-scan and mechanical sieving describes the reworked residual granite from Ernie Els Wines pit 1 as poorly graded with low plasticity.

It can be concluded that the measured PSD for medium to coarse particles is more accurate in CT-scan than in mechanical sieving. On the other hand, the measured PSD for finer particles is more accurate in mechanical sieving than CT-scanning.

Table 4-12: Mechanical properties reworked residual granite of Ernie Els Wines pit 1

Sample Properties	CT-Scan _Pit 1	Mechanical sieving Pit 1
Depth (m)	0.5	0.5
Clay (%)	0	0
Silt (%)	2	3
Sand (%)	65	71
Gravel (%)	33	26
Coefficient of uniformity (C_u)	9.4	7.1
Coefficient of curvature (C_c)	0.3	0.3
Unified Soil Classification System	ML-OL	ML-OL

4.4.5   Pore size distribution

A region of interest was selected within the scanned image by crop editing. The VGStudio Max version 2.2 imaging software was used to obtain the pore parameters using granulometry technique as described in Chapter 3. There were no mechanical methods of determining the pore size distribution to aid comparison with CT-scanning methods. Description of the pore size distribution was based on Brewer's pore classification in Table 4.4. Figure 4.12 and 4.13 shows the pore distribution of the reworked residual granite and the residual Malmesbury shales respectively. The void size (in millimeters) was determined from the size of all combined macropores in each sample.

74
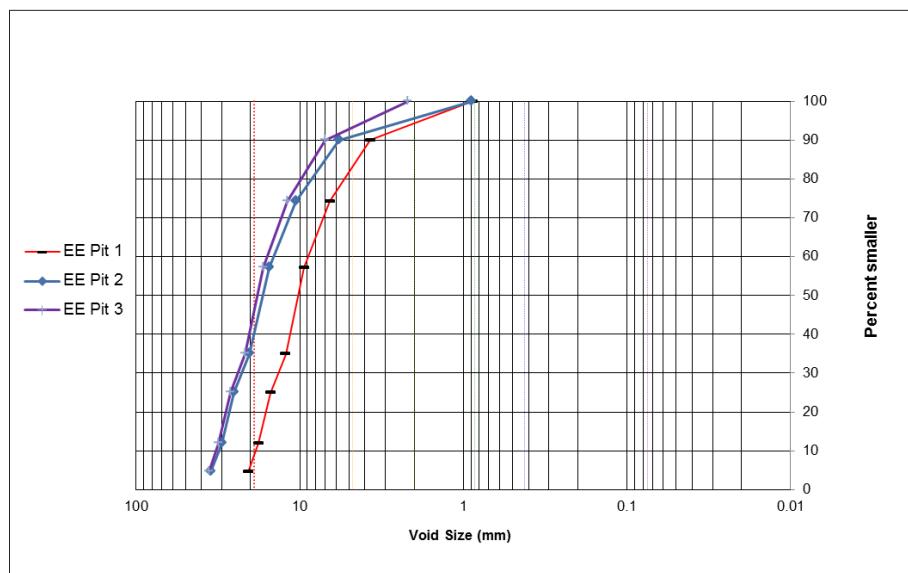
Figure 4-12: Pore size distribution of undisturbed soil samples from Ernie Els Wines.

From Figure 4.12, the minimum pore diameter of pit 1 is 0.86 mm (very fine macropores) and the maximum measured pore diameter being 20.7 mm (coarse macropores). The very fine macropores represents only 1.02% of the total pore size distributions. The medium macropores represents about 13% and the coarse macropores 80% of the total pore size distribution. The pore size distribution of Ernie Els pit 1 can be described as poorly distributed with very fine to coarse macropores.

The minimum measured void diameter for pit 2 from Figure 4.12 is 0.88 mm with the maximum void diameter as 34.92 mm. The very fine macropores represents less than 1% of the total pore size distribution. The coarse macropores makes up about 90% of the total pore size distribution with the remaining 5% representing the medium macropores. According to Brewer's classification, the pore network of Ernie Els pit 2 can be described as poorly distributed with very fine to coarse macropores.

The pores within Ernie Els pit 3 can be described as poorly distributed with fine to coarse macropores. This is because 91% of the total pore size distribution is made up of coarse macropores with the remaining 8% comprising of the fine and medium macropores with absolutely no very fine macropores.

It can be concluded that the pore size distribution corresponds with the particle size distribution of the reworked residual granite and the volumetric analysis in Table 4.5 to Table 4.7.

75
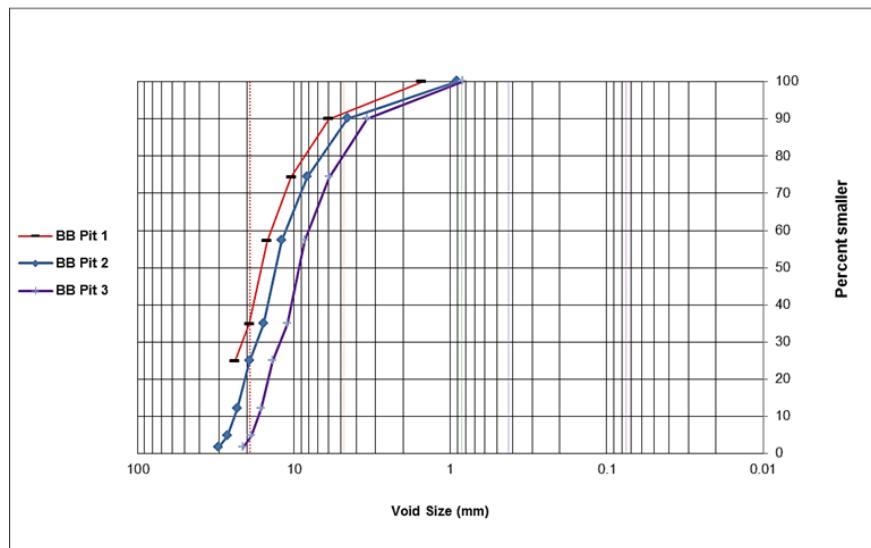
Figure 4-13: Pore size distribution of undisturbed soil samples from Boland Bricks.

From Figure 4.13, the pore size distribution of Boland Bricks pit 1 can be described as poorly distributed with no very fine macropores and as well as no medium macropores. The fine macropores represents 2.02% of the total pore distribution and the remaining 97.98% represents the coarse macropores. The minimum and maximum measured pore diameter is 1.53 mm and 23.78 mm respectively.

The minimum pore diameter in the microstructure of pit 2 is 0.91 mm and the maximum pore diameter as 37.60 mm. The very fine macropores represents only 0.43% of the total pore distribution, 2.16% medium macropores, and the remaining 97.41% represents the coarse macropores. The pore size distribution of Boland Bricks pit 2 can be described as poorly distributed with medium to coarse macropores.

For pit 3, the coarse macropores constitutes 97.17% of the total pore size distribution, 2.27% constitutes the medium macropores and the remaining 0.56% represents the very fine macropores. The pores of Boland Bricks pit 3 can be described as poorly distributed with medium to coarse macropores.

The macropores within the microstructure of the residual Malmesbury shale depicted an intergranular pore distribution, thus reducing the pore connectivity, which is a major contributing factor in the formation of a collapsible grain structure and collapse settlement as well. This is shown in Figure 4.14 (b).
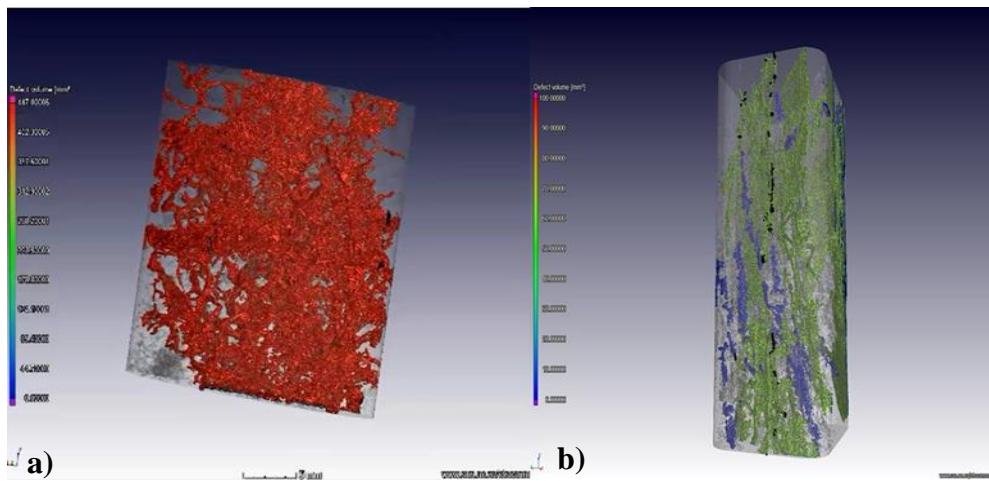
Figure 4-14: 3D pore distribution, a) reworked residual granite, and b) residual Malmesbury shale.

4.5   SEM RESULTS

4.5.1   Particle shape

The particle shape influences the void ratio, particle arrangement, and interparticle contacts of a soil fabric (Ashmawy 2003). In effect, the formation of a collapse fabric is dependent on the geometric shapes of the individual particles that make up the soil. The particle shape was evaluated based roundness/angularity. Presented in Table 4.13 through Table 4.18 is the summary of the particle shape description of the reworked residual granites and residual Malmesbury shale respectively. Description of the particle shape is done with 2D images viewed in plan, as opposed to 3D images.

77

Table 4-13: Mean roundness and shape description of particles from Ernie Els Wines Pit 1.

Particle Size Retained (mm)	Number of particles (f)	Arithmetic mean roundness	Description
> 4.75	8	0.3	Sub-rounded
2	6	0.3	Sub-rounded
0.85	7	0.4	Rounded
0.425	5	0.4	Rounded
0.25	7	0.3	Sub-rounded
0.15	9	0.4	Rounded
0.075	8	0.3	Sub-rounded
< 0.075	8	0.3	Sub-rounded

The roundness value of the particles from pit 1 (Table 4.13) is between 0.30 and 0.4. The particle shape of the soil sampled from pit 1 can be described as sub-rounded to rounded.

Table 4-14: Mean roundness and shape description of particles from Ernie Els Wines Pit 2

Particle Size Retained (mm)	Number of particles (f)	Arithmetic mean roundness	Description
> 4.75	4	0.3	Sub-rounded
2	5	0.3	Sub-rounded
0.85	8	0.2	Sub-angular
0.425	7	0.3	Sub-rounded
0.25	10	0.3	Sub-rounded
0.15	9	0.3	Sub-rounded
0.075	9	0.3	Sub-rounded
< 0.075	8	0.2	Sub-angular

From Table 4.14, a set of sixty (60) different particle shapes was analyzed. The set varies in roundness from 0.2 to 0.4. The particle shape from pit 2 can be described as sub-angular to sub-round. According to Ashmawy, (2003), angular particles can form a collapsible fabric due to an internal arching phenomenon. The particle shapes of soil sampled from pit 2 might have contributed to a higher collapse settlement compared to that of pit 1 and pit 3 as suggested by Ashmawy, (2003). The sub-angular to sub-rounded particles also led to the formation of an arching phenomenon creating well connected voids with larger average volumes.

Table 4-15: Mean roundness and shape description of particles from Ernie Els Wines Pit 3.

Particle Size Retained (mm)	Number of particles (f)	Arithmetic mean roundness	Description
> 4.75	7	0.4	Rounded
2	3	0.4	Rounded
0.85	5	0.3	Sub-rounded
0.425	8	0.3	Sub-rounded
0.25	9	0.3	Sub-rounded
0.15	8	0.3	Sub-rounded
0.075	9	0.3	Sub-rounded
< 0.075	8	0.3	Sub-rounded

From Table 4.15, a set of fifty-eight (58) particles analyzed vary in roundness from 0.3 to 0.4 and therefore can be described as sub-rounded to rounded. The shapes of particles from pit 3 had similar attributes as to that of pit 1. The sub-rounded particles formed a collapsible fabric, but with narrowed voids. The average volume of the voids before the collapse was smaller compared to that of pit 2. Moreover, pit 3 had more sub-rounded particles compared to the particle of pit 1 and hence the initial average volume (379.36 mm^3) of pit 3 was greater than the initial average volume (313.26 mm^3) of pit 1.

Table 4-16: Mean roundness and shape description of particles from Boland Bricks Pit 1.

Number of particles (f)	Arithmetic mean roundness	Description
25	0.5	Well rounded
15	0.4	Rounded
10	0.3	Sub-rounded

A set of fifty (50) particles of different shapes were analyzed (see Table 4.16). The shape of the particles of Boland Bricks pit 1 can be described as sub-rounded to well-rounded with the mean roundness varying from 0.3 to 0.5.

Table 4-17: Mean roundness and shape description of particles from Boland Bricks Pit 2.

Number of particles (f)	Arithmetic mean roundness	Description
20	0.5	Well rounded
15	0.4	Rounded
15	0.3	Sub-rounded

From Table 4.17, a set of fifty (50) different particle shapes was analyzed and vary in mean roundness from 0.3 to 0.5. Therefore, the shape of particles of Boland Bricks pit 2 can be described as sub-rounded to well-rounded.

Table 4-18: Mean roundness and shape description of particles from Boland Bricks Pit 3.

Number of particles (f)	Arithmetic mean roundness	Description
25	0.5	Well rounded
15	0.4	Rounded
15	0.3	Sub-rounded

The mean roundness of the shape of particles in Table 4.18 varies from 0.3 to 0.5. A total of fifty-five particles of different shapes were analyzed. The shape of the particles of Boland Bricks pit 3 can be described as sub-rounded to well-rounded.

The shape of the particles (residual Malmesbury shales) from the three (3) pits of Boland Bricks contributed to the non-collapsible behavior. This is because the rounded coarser particles are coated with clay and also surrounded by other sub-rounded and platy particle which leads to the formation of a tighter packing arrangement. This renders the microstructure non porous.

In addition, the coarse particles were coated with illite, a non-expandable clay. The thin, plate-like, and flaky nature of the illite and the irregular shape of the surrounding particles resulted in the formation of an intergranular pore system. Figure 4.15 shows a coarse particle coated with clay minerals.

It can be concluded that, porosity and pore size decreases with decreasing sphericity of the overall particle shape, and this directly affects the formation of a collapsible grain structure within the residual Malmesbury shales of Boland Bricks (Fraser, 1935).
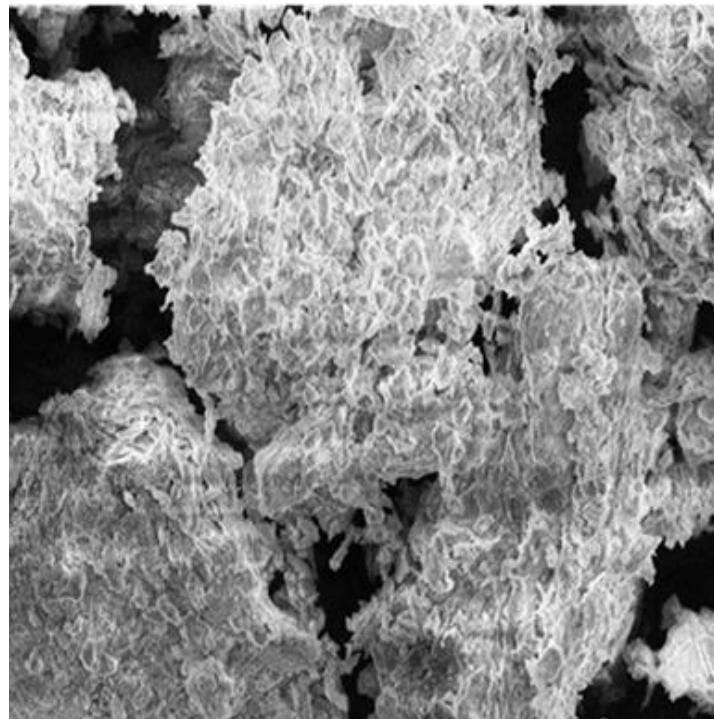
Figure 4-15: A microscopic view of a coarse sand particle coated with illite.

4.5.2   Soil mineral composition

The mineralogy of a soil plays a major role in soil characterization, and the formation of clay minerals. The chemical composition of the original or parent rock determines the mineral composition of the resulting soil formed from the weathering process (Reddy and Inyang, 2000). To obtain the compositional data, each polished and coated soil sample was subjected to energy-dispersive x-rays. This process is termed energy-dispersive spectrometry (EDS) analysis. The detail of the EDS analysis is documented in Chapter 3. Table 4.19 and Table 4.20 give details of the mineral composition of the reworked residual granites and the residual Malmesbury shale. The mineral composition of the residual Malmesbury shale was done at the University of the Western Cape (UWC). The system at UWC is not set up for quantitative analysis as that of the University of Stellenbosch (US) lab. Therefore; the residual Malmesbury shale data are presented as semi-quantitatively which is enough to give mineral compositions and mineral identification in each sample.

4.5.2.1 Ernie Els Wines reworked residual granite mineralogy

From Table 4.19, quartz (SiO_2) is the dominant primary mineral within the soil. The graph in Figure 4.4 shows that the reworked residual granite soil specimens displayed signs of swelling upon saturation at 200 kPa. The swelling is due to the presence of smectite, an expansive clay mineral that bridged the particles together.

Another observation is that the percentage of clay fractions within the reworked residual granites determines the severity of collapse. The higher the clay content, the higher the amount of smectite and therefore, the lower the severity of collapse. The expansive nature of the smectite enhances a potentially collapsible soil to distribute stresses upon loading and saturation before collapse finally occurs.

To conclude, the rounded and sub-rounded coarse quartz within the soils are coated and bridged together by clays which are easily eroded and leached out. The morphology of the particle results in higher porosity and an open texture, thus becoming susceptible to collapse. The extent of collapse is also influenced by smectite. Figure 4.16 shows the microstructure of the EE reworked residual granite.
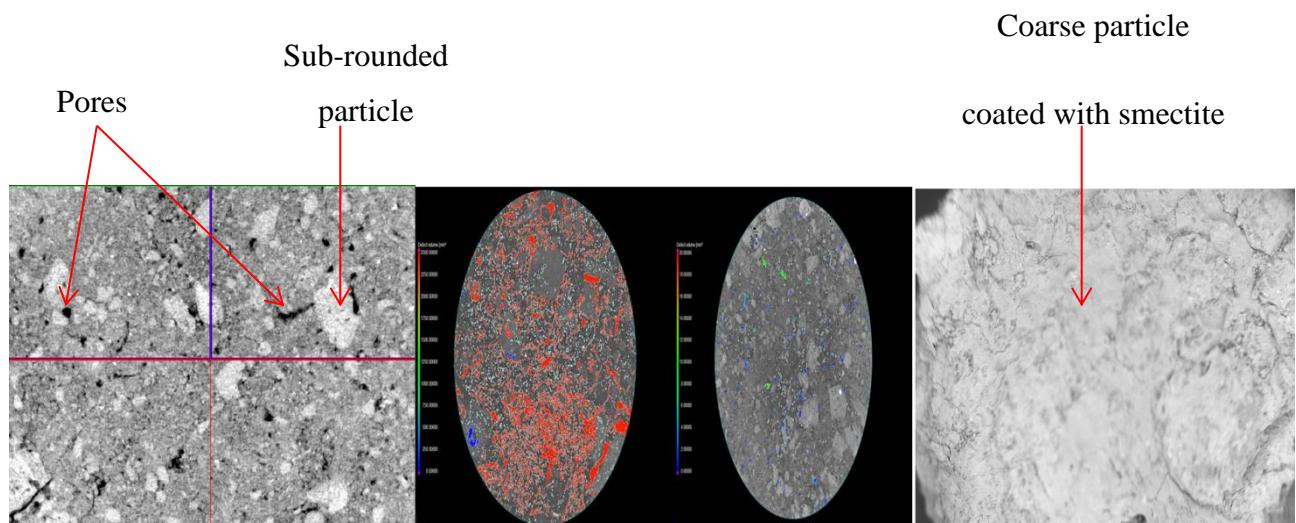
Figure 4-16: The microstructure of EE reworked residual granite.

4.5.2.2   Boland Bricks residual Malmesbury shale mineralogy

From Table 4.20 below, the Boland Bricks residual Malmesbury shale is composed of medium to fine grained quartz which is the dominant mineral. Secondary minerals kaolinite and illite were detected by SEM using EDS analysis. The secondary minerals cements the medium grained quartz particles together. The residual Malmesbury shales depicted a more ductile behavior instead of collapse behavior. This can be attributed to the laminated texture of the clay component (illite and kaolinite).

It can be concluded that, rounded and sub-rounded quartz is covered by illite and also surrounded by irregular kaolinite as well as laminated clays. These make the particles tightly packed with low porosity, thus not being susceptible to collapsible.

Table 4-19: Reworked residual granite mineral composition, Ernie Els Wines.

Primary minerals	Chemical composition	Wt % Si	Wt% O	Wt% K	Wt% Al	Wt% Ca	Wt% Na	Wt% Fe	Wt% Ti	Wt% Mg	Wt% Mn
Quartz	SiO_2	46.24	52.92								
Orthoclase feldspar	$KAlSi_3O_8$	30.30	46.19	13.27	9.93	-	-				
Plagioclase feldspar	$(Ca,Na)\ AlSi_3O_8$	31.54	48.57	0.09	10.56	0.13	9.11				
Secondary minerals											
Kaolinite	$(Si_4)\ Al_4O_{10}(OH)_8$	46.54	52.20		0.33	-	-				
Smectitie	$(Na, Ca)(Al,Mg)_6(Si4010)_3(OH)_6$	27.29	45.47	0.30	10.20			15.53		1.17	
Other minerals											
Astrophyllite	$(K,Na)_3(Fe,Mn)_7Ti_2(SiO_3)_8(O,OH)_7$	8.72	40.85	2.42	3.80		0.11	4.67	37.70		1.55

Table 4-20: Residual Malmesbury shale mineral composition, Boland Bricks.

Primary minerals	Chemical composition	Wt % Si	Wt% O	Wt% K	Wt% Al	Wt% Fe	Wt% Ti	Wt% Mg
Quartz	SiO_2	36.04	41.17					
Secondary minerals								
Kaolinite	$(Si_4)\ Al_4O_{10(}OH)_8$	14.88	39.79		7.55			
Illite	K, Al, Mg, Fe, (SiO)	12.58	37.09	1.48	9.86	6.95	0.72	0.42

CHAPTER 5. CONCLUSION AND RECCOMENDATION

The main objective of this research was to develop a test procedure using CT-scanning and SEM to investigate the microstructure of potentially collapsible soils. The soil sample types used for this study included reworked residual granites from Ernie Els Wines, Stellenbosch, and residual Malmesbury shales from Boland Bricks, Paarl. The aim of this study was achieved through the test procedures developed using CT-scanning and SEM, and experimental work which included collapse potential testing. The particle size distribution for SEM was not achieved. Moreover, there were no mechanical means to determine the pore size distribution.

5.1   INFERENCES AND CONCLUSIONS

The first objective of this research was to perform the traditional Geotechnical laboratory tests to set a baseline for comparison. The following inferences can be drawn from the indicator analysis and the collapse potential test:

- The results obtained from the collapse potential tests were used to establish a relationship between the severity of collapse settlement and the percentage of clay present in the soil. It was deduced that a lower percentage of clay increased the severity of collapse.
- At specific stress levels the difference between percentage of sand and clay in the soil sample is directly proportional to the collapse potential. The greater the difference between the sand and clay fractions, the higher the collapse potential.
- The results from the collapse potential test confirmed that the reworked residual granite from Ernie Els is highly susceptible to collapse settlement. Therefore, further investigation should be carried out when dealing with the foundations of structures within the vicinity of Ernie Els Wines.

The second objective of this study was to use CT-scanning and SEM to execute scans on the two soil types, i.e. the reworked residual granite and residual Malmesbury shales. The following deductions can be drawn from the images produced by the scanning process:

- The results from this research indicates that the General Electric Phoenix VTomeX L240 X-ray micro computed tomography scanner (microCT), the NanoCT, and the ZEISS EVO

MA15 scanning electron microscope at the center for analytical facility of the University of Stellenbosch is capable of performing quality scans of higher resolutions.

- The quality of the scan resolution was dependent on the diameter of the canister as well as its thickness. Results from the CT-scanning indicate that smaller sized canisters produce high-quality images.

The third objective was achieved by developing image processing techniques to determine the particle and pore size distribution, particle shape, and the volumetric change (porosity). In addition, the energy-dispersive spectroscopy (EDS) analysis was employed to determine the mineral composition of the two soil types used for this study. The two procedures employed resulted in the following deductions:

- Image analysis is a very useful tool for the characterization of the microstructure of soils.
- The measured particle size distribution by CT-scanning corresponded well with the measured mechanical sieving, although the finer particles tend to blend together.
- Collapse usually occurs within the macropores of soils with a collapsible grain structure.
- The measured pore size distribution corresponded well with the measured particle size distribution by CT-scanning.
- Results from the mineral composition confirm that the type of clay mineral present in the reworked residual granite determines the severity of collapse settlement. Expansive clay minerals are able to sustain higher stresses and therefore reduce the severity of collapse settlement.
- Results from the shape analysis also confirmed that within the reworked residual granite, the severity of collapse settlement decreases with decreasing angularity of particle shape.
- Results from the shape analysis confirmed that the platy nature and the preferred orientation of the clay particles within the residual Malmesbury shales makes it resistant to collapse.

5.2   RECOMMENDATIONS

The experimental approach and procedures developed for this study has clearly established that CT-scanning and SEM can be alternate methods to determine and investigate the microstructure of potentially collapsible soils. The following actions, as emanating from this study, must be taken:

- The number of samples for CT-scanning and SEM analysis can be increased and must be of different size fractions to gain a better understanding and to establish a better correlation between CT-scanning, SEM, and traditional laboratory tests.

- By improving the scan resolution for both CT-scanning and SEM for fine-grained soils (clay sized), results for the determination of the soil properties will be more accurate

- Pore size distribution from the 3D views using CT-scanning to validate existing pore distribution models in Geotechnical engineering and also in civil engineering must be carried out. This will enhance the microstructure study and estimation of properties such as permeability, and hydraulic conductivity.

- 3D modelling using SEM imaging at different tilt angles and voltages can be explored for microstructure studies of soils, concretes and other materials.

REFERENCES

Abell, A., Willis, K., & Lange, D. (1999). "Mercury Intrusion Porosimetry and Image Analysis of Cement-Based Materials". *Journal of Colloid and Interface Science*, vol 211, no. 1, pp. 39–44. doi:10.1006/jcis.1998.5986

Alshibli, K. A., et al. (2000). "Quantifying Void Ratio Variation in Sand Using Computed Tomography." Geotechnical Measurements - Lab and Field: *Proceedings of GeoDenver 2000 Specialty Conference*, Denver 2000: pp. 30-43.

Alshibli, K.A., et al. (2000b). "Assessment of Localized Deformations in Sand Using X-Ray Computed Tomography". *Journal of Geotechnical Testing*, vol 23, no. 3, pp. 274-299.

American Society for Testing and Materials. 2006. Annual Book of ASTM Standards,

Ashmawy, A. (2003). "Evaluating the influence of particle shape on liquefaction behavior using discrete element modelling." *Proceedings of Offshore and Polar*, pp. 1–8. Retrieved from http://e-book.lib.sjtu.edu.cn/isope2003/pdffiles/volume2/2079p542.pdf

Ayadat, T., & Hanna, A. M. (2012). "Assessment of Soil Collapse Prediction Methods". vol 25, no. 1, pp. 10–12. doi:10.5829/idosi.ije.2012.25.01b.03

Basma, A. A and Tuncer, E. R. (1992). "Evaluation and control of collapsible soils". *Journal or Geotechnical Engineering*, vol. 118, no. 10, pp. 1491-1504.

Brink, A.B.A. (1979). Engineering geology of Southern Africa, vol 1, Building Publications. Pretoria. 1979.

Brink, A.B.A. and Kantey, B.A. (1961). "Collapsible grain structure in reworked residual granite Soils in South Africa". *Proceedings, 5th International Conference SM and FE*, Paris, pp.611-614.

Conley, R. F. (1969). "Some inherent errors in hydrometer sedimentation analysis". *Powder Technology*, vol 3, no 1, pp. 102–106. doi:10.1016/0032-5910(69)80061-6

Craig, R.F., 2004. Craig's Soil Mechanics, Seventh Edition, Available at: http://books.google.ca/books/about/Craig_s_Soil_Mechanics_Seventh_Edition.

Di Stefano, C., Ferro, V., & Mirabile, S. (2010). Comparison between grain-size analyses using laser diffraction and sedimentation methods. *Biosystems Engineering*, vol 106, no. 2, pp. 205–215. doi: 10.1016/j. Biosystemseng.

Dippenaar, M., Rooy, L.V.A.N. & Croucamp, L., 2006. The use of index laboratory testing to determine the engineering behaviour of granitic saprolite. vol 466, pp. 1–4.

Dudley, J.H. (1970). "Review of collapsing soils". *Journal of the soil mechanics and foundation division*, ASCE, vol 96, SM3, pp. 925-947.

Fonseca, J., O'Sullivan, C., Coop, M. R., & Lee, P. D. (2012). "Noninvasive characterization of particle morphology of natural sands". *Soils and Foundations*, vol 52, no. 4, pp. 712–722. doi: 10.1016/j. Sand. 2012.07.011

Franck, U., & Herbarth, O. (2002). "Using scanning electron microscopy for statistical characterization of the diameter and shape of airborne particles at an urban location". *Environmental Toxicology*, vol 17, no. 2, pp. 98–104. doi: 10.1002/Tox. 10037

Fraser, H. J. (1935), Experimental study of porosity and permeability of clastic sediments: *Journal of Geology*, vol. 43, pp. 910–1010, DOI: 10.1086/jg. 1935.43. Issue-8.

Gerhart, V. J., Waugh, W. J., Glenn, E. P., & Pepper, I. L. (2004). Environmental Monitoring and Characterization. *Environmental Monitoring and Characterization*. doi:10.1016/B978-012064477-3/50021-7

Goodhew, P. J., Humphreys, F. J., & Beanland, R. (2001). Electron microscopy and analysis. *Annals of Physics*, vol 54, no. 258. Retrieved from http://books.google.com/books?

Hajnos, M.,et. al. (2006). "Complete characterization of pore size distribution of tilled and orchard soil using water retention curve, mercury porosimetry, nitrogen adsorption, and water desorption methods". *Geoderma*, vol 135, pp. 307–314. doi: 10.1016/j. geothermal. 2006.01.010

Illinois, N. (no date.). "Suspended marine clay mineral identification by scanning electron microscopy and energy-dispersive X-ray analysis". *Microscopy,* pp. 133–137.

Jennings, J.E. and Knight, K. (1975). "A guide to construction on or with materials exhibiting additional settlement due to collapse of grain structure". *Proceedings. Sixth regional conference for Africa on soil mechanics and foundation engineering*, Durban, South Africa, pp. 99- 105

Johnson, B., Leethem, J., Linton K. (1995). Effective XRF Field Screening of Lead in Soil. Proceeding Accessed from http://info.ngwa.org/gwol/pdf/950161762.PDF

Khan, A. M. (2013). "Image segmentation methods: A comparative study". *International Journal of Soft Computing and Engineering* (IJSCE), vol 3, no.4, pp. 84–92. doi:10.1117/1.2762250

Knight. K, and Dehlen. G L. (1963). "The failure of a road constructed on a collapsing soil". *Proceedings, 3rd Regional Conference for Africa SM and FE*. Salisbury.

Koerner, R.M. (1984). Construction and Geotechnical methods in foundation engineering. USA: McGraw-Hill, Inc.

Millogo, Y., Hajjaji, M., & Morel, J. C. (2011). "Physical properties, microstructure and mineralogy of termite mound material considered as construction materials". *Applied Clay Science*, vol 52, no.1-2, pp. 160–164. doi:10.1016/j.clay.2011.02.016

Nagabhushana, S. (2005). "Computer Vision and Image Processing". New Age International Publishers.

Nimmo, J. R. (2004). "Porosity and pore size distribution". *Encyclopedia of Soils in the Environment*, pp. 295–303. doi:10.1016/B978-0-12-409548-9.05265-9

Okolo, G. N., et. al (2015). "Comparing the porosity and surface areas of coal as measured by gas adsorption, mercury intrusion, and SAXS techniques". vol 141, pp. 293–304.

Polish, M. (1995). "Qualitative and quantitative analysis of microstructures in Polish glacial tills with respect to their age". vol 39, no. 3.

Ramachandran, G.N., & Lakshminarayanan, A.V. (1970). Three-dimensional reconstruction from radiographs and electron micrographs: Application of convolutions instead of Fourier transforms. *Proceedings of the National Academy of Science*, vol 68, pp. 2236-2240.

Reddy, L.N. & Inyang, H. I (2000). Geoenvironmental engineering, principles and applications. New York: Marcel Dekker, Inc.

Remley, P.A., Bradford, J.M. (1989), "Relationship of soil crust morphology to inter-rill erosion parameters", Soil science society. *American Journal*, vol 53, pp. 1215–1221.

Rogers, C.D.F. (1995). Types and Distribution of Collapsible Soils. In: Derbyshire, E., Dijkstra, T. and Smalley, I.J. (eds.) (1995). Genesis and Properties of Collapsible Soils, NATO ASI Series, *Kluwer Academic Publishers*, pp. 173-205.

Romero, E., & Simms, P. H. (2009). Microstructure investigation in unsaturated soils: A review with special attention to contribution of mercury intrusion porosimetry and environmental scanning electron microscopy. *Laboratory and Field Testing of Unsaturated Soils*, pp. 93–115. doi:10.1007/978-1-4020-8819-3_8

Russ, John C. The Image Processing Handbook, 4th ed. Boca Raton, FL: CRC Press, 2002.

Schulze. B, R. (1958) The climate of South Africa according to Thornthwaite's rational classification. *South African Geographical Journal*, Vol 40.

Schwartz, K. (1985). Collapsible Soils: Problems of Soils in South Africa, state-of-the-art. *The Civil Engineer in South Africa*, vol 27, pp. 379-393.

Shepp, L.A., Logan, B.F. (1974). Reconstructing interior head tissue from X-ray transmissions. *IEEE Transactions on Nuclear Sci*ence NS-21, pp. 228-236.

Sing, K. (2001). The use of nitrogen adsorption for the characterization of porous materials. Colloids and Surfaces A: *Physicochemical and Engineering Aspects*, vol 187-188, pp. 3–9. doi:10.1016/S0927-7757(01)00612-4

Smith et al. - 1979 - A Threshold Selection Method from Gray-Level Histograms, vol 20, no. 1, pp. 62–66.

Sprawls, P. (1995). Physical principles of medical imaging. Madison, Wis, *Medical Physics Pub*.

Sullivan, L.A. (1990). "Micropiting of some clay materials adjacent structural pores", *Geoderma*, vol 46, pp. 371–376.

Thakur, P., & Madaan, N. (2014). "A survey of image segmentation techniques". *International Journal of Research in Computer Applications and Robotics*, vol 2, no. 4, pp. 158–165.

Thompson, M., Gonzalez, R.C. & Wintz, P., (1981). Digital Image Processing, Available at: http://www.jstor.org/stable

VanCott R., McDonald, B. & Seelos, A. (1999) Standard Soil Sample Preparation Error and Comparison of PortableXRF of Laboratory AA Analytical Results. *Nuclear Instruments and Methods in Physical Research*, vol 422, pp 801-804.

Woodward, V. P., & Amjad, Z. (N.d.). Valerie P. Woodward and Zahid Amjad, pp. 387–406.

www.cs.cf.ac.uk/Dave/Vision_lecture/node34

www.ga.gov.au/about/what-we-do/facilities/laboratories/palaeontology

www.homes.di.unimi.it/ferrari/ElabImm2011_12/EI2011_12_16_segmentation_double.pdf

www.RadiologyInfo.org

www.slideshare.net/mukuljindal1/image-segmentation-17510351

APPENDICES

APPENDIX B: Collapse Potential Tests

B-1: Ernie Els Wines pit 1 sample 1

Table B-1.1: Ring properties for pit 1 sample 1

Area (mm^2)	4004.448
Height (mm)	20.00
Mass of ring (mm)	83.50
Diameter of ring (mm)	71.40
Mass of ring + dry specimen (g)	170.24
Mass of dry specimen (g)	86.74
Height of solid phase, Hs	8.023

Table B-1.2: Collapse potential test results for pit 1 sample 1

Mass on hanger (g)	Stress (kN/m^2)	Reading (mm)	ΔH= Zo-Z	H= Ho-ΔH	e=(H-Hs)/Hs
0	1	7.695	0	20.00	1.492969441
1	25	7.372	-0.323	19.68	1.452707985
2	50	7.156	-0.539	19.46	1.425783915
4	100	6.823	-0.872	19.13	1.384275973
8	200	6.836	-0.859	19.14	1.385896404
8	200	4.652	-2.720	17.28	1.153925597
16	400	4.492	-3.203	16.80	1.093720385
32	800	4.175	-3.520	16.48	1.054206819

Table B-1.3: Collapse interpretation for pit 1 sample 1

Collapse Potential (%)	9.305
Severity of problem	Trouble

95

B-2: Ernie Els Wines pit 1 sample 2

Table B-2.1: Ring properties for pit 1 sample 2

Area (mm^2)	4004.44758
Height (mm)	20.00
Mass of ring (mm)	83.50
Diameter of ring (mm)	71.40
Mass of ring + dry specimen (g)	171.35
Mass of dry specimen (g)	87.85
Height of solid phase, Hs	8.125

Table B-2.2: Collapse potential test results for pit 1 sample 2

Mass on hanger (g)	Stress (kN/m^2)	Reading (mm)	ΔH= Zo-Z	H= Ho-ΔH	e=(H-Hs)/Hs
0	1	8.232	0	20.00	1.461470339
1	25	8.153	-0.079	19.92	1.451747532
2	50	7.767	-0.465	19.54	1.404241154
4	100	7.882	-0.350	19.65	1.418394609
8	200	7.894	-0.338	19.66	1.419871491
8	200	5.964	-2.189	17.81	1.192062411
16	400	5.396	-2.836	17.16	1.112433845
32	800	5.882	-2.350	17.65	1.172247575

Table B-2.3: Collapse interpretation for pit 1 sample 2

Collapse Potential (%)	9.255
Severity of problem	Moderate Trouble

B-3: Ernie Els Wines pit 2 sample 1

Table B-3.1: Ring properties for pit 2 sample 1

Area (mm^2)	4004.44758
Height (mm)	20
Mass of ring (mm)	83.50
Diameter of ring (mm)	71.40
Mass of ring + dry specimen (g)	193.55
Mass of dry specimen (g)	110.05
Height of solid phase, Hs	10.17849739

Table B-3.2: Collapse potential test results for pit 2 sample 1

Mass on hanger (g)	Stress (kN/m^2)	Reading (mm)	ΔH= Zo-Z	H= Ho-ΔH	e=(H-Hs)/Hs
0	1	7.979	0	20	0.964926573
1	25	7.769	-0.21	19.79	0.944294844
2	50	7.538	-0.441	19.559	0.921599942
4	100	7.254	-0.725	19.275	0.893697984
8	200	7.685	-0.294	19.706	0.936042152
8	200	4.263	-3.716	16.284	0.599843215
16	400	4.233	-3.746	16.254	0.596895826
32	800	3.502	-4.477	15.523	0.525077759

Table B-3.3: Collapse interpretation for pit 2 sample 1

Collapse Potential (%)	17.11
Severity of problem	Severe trouble

B-4: Ernie Els Wines pit 2 sample 2

Table B-4.1: Ring properties for pit 2 sample 2

Area (mm^2)	4004.44758
Height (mm)	20
Mass of ring (mm)	83.50
Diameter of ring (mm)	71.40
Mass of ring + dry specimen (g)	191.89
Mass of dry specimen (g)	108.39
Height of solid phase, Hs	10.0249644

Table B-4.2: Collapse potential test results for pit 2 sample 2

Mass on hanger (g)	Stress (kN/m^2)	Reading (mm)	ΔH= Zo-Z	H= Ho-ΔH	e=(H-Hs)/Hs
0	1	7.573	0	20	0.995019553
1	25	7.493	-0.08	19.92	0.987039475
2	50	7.013	-0.56	19.44	0.939159005
4	100	7.284	-0.289	19.711	0.96619152
8	200	7.296	-0.277	19.723	0.967388532
8	200	3.537	-3.956	16.044	0.600404685
16	400	2.943	-4.630	15.37	0.533172526
32	800	2.884	-4.689	15.311	0.527287219

Table B-4.3: Collapse interpretation

Collapse Potential (%)	18.39
Severity of problem	Severe trouble

B-5: Ernie Els Wines pit 3 sample 1

Table B-5.1: Ring properties of pit 3 sample 1

Area (mm^2)	5476.70
Height (mm)	20.00
Mass of ring (mm)	83.50
Diameter of ring (mm)	71.40
Mass of ring + dry specimen (g)	193.04
Mass of dry specimen (g)	109.54
Height of solid phase, Hs	7.407809954

Table B-5.2: Collapse potential test results for pit 3, sample 1

Mass on hanger (g)	Stress (kN/m^2)	Reading (mm)	ΔH= Zo-Z	H= Ho-ΔH	e=(H-Hs)/Hs
0	1	8.519	0	20.00	1.69985328
1	25	8.286	-0.233	19.77	1.668399989
2	50	7.806	-0.713	19.29	1.60360351
4	100	7.820	-0.699	19.30	1.605493408
8	200	7.445	-1.074	18.93	1.554871159
8	200	5.264	-3.022	16.98	1.291905449
16	400	4.675	-3.844	16.16	1.180941479
32	800	3.885	-4.634	15.37	1.074297275

Table 5.3: Collapse interpretation for Ernie Els pit 3, sample 1

Collapse Potential (%)	9.74
Severity of problem	Trouble

103

B-6: Ernie Els pit 3 sample 2

Table B-6.1: Ring properties for pit 3 sample 2

Area (mm^2)	4005.47
Height (mm)	20.00
Mass of ring (mm)	83.50
Diameter of ring (mm)	71.40
Mass of ring + dry specimen (g)	174.00
Mass of dry specimen (g)	90.50
Height of solid phase, Hs	8.37

Table B-6.2: Collapse potential test results for pit 3 sample 2

Mass on hanger (g)	Stress (kN/m^2)	Reading (mm)	ΔH= Zo-Z	H= Ho-ΔH	e=(H-Hs)/Hs
0	1	7.948	0	20.00	1.390002511
1	25	6.698	-1.250	18.75	1.240627355
2	50	6.343	-1.605	18.40	1.19820481
4	100	6.343	-1.605	18.40	1.19820481
8	200	6.348	-1.600	18.40	1.198802311
8	200	3.753	-2.945	17.06	1.038074642
16	400	4.575	-3.373	16.63	0.986928588
32	800	4.568	-3.380	16.62	0.986092087

Table B-6.3: Collapse interpretation

Collapse Potential (%)	6.725
Severity of problem	Trouble

105

Boland Bricks

B-7: Boland Bricks pit 1 sample 1

B-7.1: Ring properties for pit 1 sample 1

Area (mm^2)	2009.57
Height (mm)	20.00
Mass of ring (mm)	50.40
Diameter of ring (mm)	50.58
Mass of ring + dry specimen (g)	115.0
Mass of dry specimen (g)	64.60
Height of solid phase, Hs	11.91

Table B-7.2: Collapse potential test results for pit 1 sample 1

Mass on hanger (g)	Stress (kN/m^2)	Reading (mm)	ΔH= Zo-Z	H= Ho-ΔH	e=(H-Hs)/Hs
0	1	7.544	0	20.00	0.679829026
1	25	7.242	-0.302	19.70	0.654463608
2	50	6.839	-0.705	19.30	0.620615053
4	100	6.555	-0.989	19.01	0.596761481
8	200	6.175	-1.369	18.63	0.564844729
8	200	5.822	-1.420	18.58	0.560561165
16	400	5.458	-2.086	17.91	0.504622859
32	800	4.637	-2.907	17.09	0.435665877

Table B-7.3: Collapse interpretation

Collapse Potential (%)	0.255
Severity of problem	No Trouble

107

B-8: Boland Bricks pit 1 sample 2

Table B-8.1: Ring properties for pit 1 sample

Area (mm^2)	2009.57
Height (mm)	20.00
Mass of ring (mm)	50.40
Diameter of ring (mm)	50.58
Mass of ring + dry specimen (g)	115.5
Mass of dry specimen (g)	65.10
Height of solid phase, Hs	11.998

Table B-8.2: Collapse potential test results for pit 1 sample 2

Mass on hanger (g)	Stress (kN/m^2)	Reading (mm)	ΔH= Zo-Z	H= Ho-ΔH	e=(H-Hs)/Hs
0	1	7.905	0	20.00	0.666927113
1	25	7.31	-0.595	19.41	0.617336032
2	50	7.131	-0.774	19.23	0.602417034
4	100	6.951	-0.954	19.05	0.58741469
8	200	6.676	-1.229	18.77	0.564494442
8	200	6.351	-0.959	19.04	0.586997958
16	400	5.503	-2.402	17.60	0.466729167
32	800	4.564	-3.341	16.66	0.388466939

Table B-8.3: Collapse interpretation for pit 1 sample 2

Collapse Potential (%)	-1.35
Severity of problem	No Trouble

109

B-9: Boland Bricks pit 2

Table B-9.1: Ring properties for pit 2 sample 1

Area (mm^2)	5476.70
Height (mm)	20
Mass of ring (mm)	71.40
Diameter of ring (mm)	83.50
Mass of ring + dry specimen (g)	210.5
Mass of dry specimen (g)	139.10
Height of solid phase, Hs	9.41

Table B-9.1: Collapse potential tests results for pit 2 sample 1

Mass on hanger (g)	Stress (kN/m^2)	Reading (mm)	ΔH= Zo-Z	H= Ho-ΔH	e=(H-Hs)/Hs
0	1	7.651	0	20	1.126110196
1	25	7.343	-0.308	19.69	1.093368099
2	50	7.314	-0.337	19.663	1.090285239
4	100	7.145	-0.506	19.494	1.072319608
8	200	6.922	-0.729	19.271	1.048613479
8	200	6.708	-0.635	19.365	1.058606197
16	400	6.294	-1.357	18.643	0.981853619
32	800	5.791	-1.86	18.14	0.928381948

Table B-9.2: Collapse interpretation

Collapse Potential (%)	-0.47
Severity of problem	No Trouble

111

B-10: Boland Bricks pit 2 sample 2

Table B-10.1: Ring properties of pit 2 sample 2

Area (mm^2)	5476.70
Height (mm)	20
Mass of ring (mm)	71.40
Diameter of ring (mm)	83.50
Mass of ring + dry specimen (g)	201.50
Mass of dry specimen (g)	120.49
Height of solid phase, Hs	8.15

Table B-10.2: Collapse potential test results for pit 2 sample 2

Collapse Potential (%)	0.89
Severity of problem	No Trouble

B-11: Boland Bricks pit 3

Table B-11.1: Ring properties for pit 3 sample 1

Area (mm^2)	5476.70
Height (mm)	20.00
Mass of ring (mm)	83.50
Diameter of ring (mm)	71.40
Mass of ring + dry specimen (g)	202.50
Mass of dry specimen (g)	131.10
Height of solid phase, Hs	8.87

Table 11.2: Collapse potential test results for pit 3 sample 1

Mass on hanger (g)	Stress (kN/m^2)	Reading (mm)	$\Delta H = Z_o - Z$	$H = H_o - \Delta H$	$e = (H - H_s)/H_s$
0	1	7.162	0	20.00	1.255849949
1	25	7.079	-0.083	19.92	1.246488171
2	50	6.942	-0.22	19.78	1.231035599
4	100	6.730	-0.432	19.57	1.20712359
8	200	6.397	-0.765	19.24	1.169563688
8	200	6.239	-0.840	19.16	1.161104251
16	400	5.883	-1.279	18.72	1.111588344
32	800	5.410	-1.752	18.25	1.058237493

Table B-11.3: Collapse interpretation for pit 3 sample 1

Collapse Potential (%)	0.375
Severity of problem	No trouble

114

B-12: Boland Bricks pit 3

Table B-12.1: ring properties of pit 3 sample 2

Area (mm^2)	5478.10
Height (mm)	20.00
Mass of ring (mm)	71.40
Diameter of ring (mm)	83.50
Mass of ring + dry specimen (g)	202.50
Mass of dry specimen (g)	131.10
Height of solid phase, Hs	8.86

Table B-12.2: Collapse potential test results for pit 3 sample 2

Mass on hanger (g)	Stress (kN/m^2)	Reading (mm)	ΔH= Zo-Z	H= Ho-ΔH	e=(H-Hs)/Hs
0	1	7.725	0	20.00	1.256424322
1	25	7.464	-0.261	19.74	1.226977984
2	50	7.264	-0.461	19.54	1.204413741
4	100	7.017	-0.708	19.29	1.176546901
8	200	6.710	-1.015	18.99	1.141910787
8	200	6.460	-1.004	19.00	1.143151821
16	400	5.999	-1.726	18.27	1.061694903
32	800	5.378	-2.347	17.65	0.991632927

Table B-12.3: Collapse interpretation

Collapse Potential (%)	-0.055
Severity of problem	No trouble

116

APPENDIX C: **CT-Scanning**

Using Avizo Fire, version 8.0 for PSD.

- Loading in the reconstructed image data;

- Volume rendering;

- Thresholding the volume rendered;

- Select region of interest (ROI) by Crop editing: Here the material region is cropped to remove external air. For this study, same 3D image with the dimension (750 mm x 750 mm x 150 mm) was maintained throughout the analysis;

- Non-local means filtering - to smoothen the data;

- Interactive thresholding - to create a grayscale image;

- Select Separate objects - to extract the particles to be analyzed;

- Label analysis - volume render and data saved and;

- Sieve analysis – to retrieve the geometric properties of individual particles.

Image analysis using the VGStudio Max 2.2.

- Loading in the reconstructed image data;

- Select region of interest (ROI) by Crop editing;

- Extract the ROI;

- Interactive thresholding - to create a grayscale image;

- Surface determination – to mark out the edges of the thresholded image (pores);

- Defect analysis – to highlight pores by color coding and to view internal features;

- Extract data and export to excel.

APPENDIX D: SEM

Carbon coating instrument

Carbon coating procedure

1. Prepare carbon coater
   - Loosen screws and remove old carbon rods;
   - Brush and clean glass chamber, and carbon rod holder.
2. Prepare carbon rods
   - Sand flat the carbon rods with sand paper;
   - Sharpen the rods until the front point is about 5mm in length.
3. Load carbon rods and samples
   - Place the rods into the appropriate holder;
   - Mount sample on the stage in the glass chamber;
   - Close the lid of the glass chamber and select "QT Pulse Rod Evap" on the control panel to start coating process.

ZIESS EVO MA15 instrument

Sample imaging using ZIESS EVO MA15

1. Start up EVO instrument and computer.
2. Start up the EVO software (Inca-Wave-Microscope).
3. In Inca-Wave-Microscope setup, right click the Gate –valve to close.
4. Vent the sample chamber.
5. Flush the sample chamber with Nitrogen gas (N_2) : chamber opens automatically
6. Mount carbon coated sample on the sample stage: close chamber
7. Pump out excess air and close N_2 cylinder valve.
8. Select "Beam on" when vacuum status indicates "ready".
9. Adjust magnification, brightness, contrast, and scan speed till the ROI is in focus.
10. Perform the analysis of interest (x-ray microanalysis, digital image analysis, and quantitative analysis).